

**Analysis of Eelgrass in Padilla Bay, Washington Using an Uncrewed Aerial System**

By

Hannah Hein

Accepted in Partial Completion  
Of the Requirements for the Degree  
Master of Science

ADVISORY COMMITTEE

Dr. David Wallin, Chair

Dr. Sylvia Yang

Dr. Andrew Bunn

GRADUATE SCHOOL

David L. Patrick, Dean

## **Master's Thesis**

In presenting this thesis in partial fulfillment of the requirements for a master's degree at Western Washington University, I grant to Western Washington University the non-exclusive royalty-free right to archive, reproduce, distribute, and display the thesis in any and all forms, including electronic format, via any digital library mechanisms maintained by WWU.

I represent and warrant this is my original work and does not infringe or violate any rights of others. I warrant that I have obtained written permission from the owner of any third party copyrighted material included in these files.

I acknowledge that I retain ownership rights to the copyright of this work, including but not limited to the right to use all or part of this work in future works, such as articles or books.

Library users are granted permission for individual, research, and non-commercial reproduction of this work for educational purposes only. Any further digital posting of this document requires specific permission from the author.

Any copying or publication of this thesis for commercial purposes, or for financial gain, is not allowed without my written permission.

Hannah Hein

24 May 2022

# **Analysis of Eelgrass in Padilla Bay, Washington Using an Uncrewed Aerial System**

A Thesis  
Presented to  
the Faculty of  
Western Washington University

In Partial Fulfillment  
Of the Requirements for the Degree  
Master of Science

By  
Hannah Hein  
May 2022

## Abstract

Eelgrass is an important part of coastal environments in the Pacific Northwest as it provides crucial habitat and moderates storm surge. Padilla Bay, Washington is home to one of the largest eelgrass meadows in North America and contains the native *Zostera marina* and the non-native *Z. japonica*. The relationship between these two species is of interest due to the influx of *Z. japonica* in previously unvegetated areas. I used an uncrewed aerial system (UAS) and a multispectral camera to study species dynamics. I compared the ability of values derived from the band data, two vegetation indices, and a principal components analysis (PCA) to predict eelgrass cover using pixel- and object-based methods. In the pixel-based analysis, using a red and red edge band in a multiple linear regression was the best way to estimate overall percent cover for the full season ( $R^2 = 0.79$ ). Regressions used to predict *Z. marina* ( $R^2=0.55$ ) and *Z. japonica* ( $R^2=0.32$ ) cover individually performed poorly. In the object-based analysis, using band means and standard deviations in a support vector machine (SVM) classification resulted in an overall accuracy of 78.3%. This method performed the best at classifying segments based on dominant species, with user's accuracies for *Z. marina* and *Z. japonica* of 80% and 100%, respectively. PCA-informed segmentation and classification also performed well, with an overall accuracy of 70.6%. Conducting object-based image segmentation with the Micasense Dual Camera System and SVM classification may be a promising method for identifying spectral differences between *Z. marina* and *Z. japonica*.

## **Acknowledgements**

This project would not have been possible without the help of my advisor, Dr. David Wallin and committee members Dr. Sylvia Yang and Dr. Andrew Bunn. I truly appreciate their feedback and advice in forming, conducting, and writing this thesis. I would also like to thank the Padilla Bay National Estuarine Research Reserve, particularly Suzanne Shull and Heath Bohlmann, for their expertise on Padilla Bay and for sharing their monitoring data. This project required lots of field assistance, and I would like to thank Carl Franz, Charles Linneman, Scott Linneman, Rachel Yonemura, Maggy Critchlow, Grace Freeman, Matt Roberts, and Emma Sharpe for their hours helping with ground control and field collections. This work was funded by the Western Washington University Department of Environmental Science and the Borman Assistantship through the Padilla Bay Foundation.

## Table of Contents

Abstract .....	iv
Acknowledgements .....	v
List of Figures .....	x
List of Tables .....	xi
1.0   Introduction .....	1
1.1   Eelgrass in the Pacific Northwest.....	1
1.2   Ground monitoring efforts.....	3
1.3   Remote sensing for seagrass monitoring .....	4
1.4   Research goals .....	6
2.0   Methods .....	8
2.1   Study area .....	8
2.2   Permanent monitoring plots .....	10
2.3   UAS flights .....	10
2.3.1   Equipment .....	10
2.3.2   Flight path development.....	12
2.3.3   Scheduling flights .....	13
2.3.4   Flight protocol .....	13
2.4   Biological sampling .....	14
2.4.1   Plot selection .....	14

2.4.2   Percent cover .....	15
2.4.3   Epiphyte measurements .....	15
2.5   Image processing .....	16
2.6   Calculation of PCA, NDVI, and NDRE .....	17
2.7   Object-based image analysis .....	18
2.8   Statistical analysis .....	19
3.0   Results .....	22
3.1   Image quality .....	22
3.1.1   Sun glint .....	22
3.1.2   Optimal flight parameters .....	25
3.2   Epiphyte load .....	28
3.3   Principal component analysis .....	30
3.4   Pixel-based analysis .....	32
3.4.1   Total eelgrass cover .....	32
3.4.2   <i>Z. japonica</i> cover .....	34
3.4.3   <i>Z. marina</i> cover .....	34
3.5   Object-based image analysis .....	39
3.5.1   Accuracy of object-based image analysis methods .....	40
3.5.2   Mapping object-based image analysis results .....	44
4.0   Discussion .....	53

4.1   Image collection and quality .....	53
4.2   Impact of epiphyte load .....	56
4.3   Principal components analysis .....	57
4.3.1   Brightness index .....	57
4.3.2   Vegetation index .....	58
4.3.3   PC3 .....	59
4.4   Pixel-based models to predict percent eelgrass cover .....	59
4.5   Object-based image segmentation .....	61
4.6   Conclusion .....	65
5.0   Works Cited .....	67
6.0   Appendices .....	73
6.1   Image processing workflow in Agisoft Metashape .....	73
6.1.1   Loading imagery and calibrating reflectance .....	73
6.1.2   Aligning photos .....	74
6.1.3   Error reduction .....	76
6.1.4   Building the dense point cloud, mesh, digital elevation model, and orthomosaic ...	77
6.2   Parameters used in ENVI workflow for PCA .....	79
6.3   Imagery .....	80
6.4   Object-based image analysis supplemental results .....	83
6.4.1   Band segmentation .....	83



6.4.2   NDRE segmentation .....	86
6.4.3   NDVI segmentation .....	88
6.4.4   PCA segmentation.....	91
6.5   Camera comparison .....	93
6.5.1   Objective .....	93
6.5.2   Methods.....	94
6.5.3   Results .....	95

## List of Figures

Figure 1: Overview of study site at Padilla Bay, WA.....	9
Figure 2: Map of permanent plots and UAS flight extent .....	11
Figure 3: Comparison of Micasense, Landsat 8, and Worldview 2 bands .....	12
Figure 4: Near infrared images at different tides .....	27
Figure 5: Epiphyte load by date .....	29
Figure 6: Epiphyte load by depth.....	29
Figure 7: Epiphyte load by depth for <i>Z. marina</i> in August.....	30
Figure 8: Predicted area for cover types using band and PCA segmentations .....	47
Figure 9: Map of predicted cover using band means and sd.....	48
Figure 10: Map of predicted cover using band means .....	49
Figure 11: Map of predicted cover using PCA means .....	50
Figure 12: Map of predicted cover using PCA means and sd.....	51
Figure 13: Image of <i>Z. japonica</i> dominated area in zone 5 .....	52
Figure 14: Orthomosaics from June 7, 2020.....	80
Figure 15: Orthomosaics from June 23, 2020.....	80
Figure 16: Orthomosaics from July 4, 2020 .....	81
Figure 17: Orthomosaics from July 21, 2020 .....	81
Figure 18: Orthomosaics from August 1, 2020 .....	82
Figure 19: Orthomosaics from August 18, 2020 .....	82

## List of Tables

Table 1: Padilla Bay monitoring zones .....	8
Table 2: Micasense Dual Camera Imaging System band specifications .....	11
Table 3: Variables used in statistical modeling .....	20
Table 4: Summary of imagery used in full season dataset.....	24
Table 5: Imagery collection dates, times, and environmental conditions .....	26
Table 6: Actual and theoretical dates at optimal flight conditions .....	27
Table 7: PCA loadings for full season .....	31
Table 8: PCA loadings for July 4.....	32
Table 9: Summary of regression models for total eelgrass cover .....	35
Table 10: Regression model equations for total eelgrass cover.....	36
Table 11: Summary of regression models for <i>Z. japonica</i> cover.....	37
Table 12: Summary of regression models for <i>Z. marina</i> cover .....	38
Table 13: Categorization criteria for ground truth plots .....	40
Table 14: Summary of classification accuracies for categorization methods.....	41
Table 15: User's, producer's, and overall accuracy for four segmentation types.....	43
Table 16: Predicted area and producer's accuracy for band and PCA segmentations.....	46
Table 17: Parameters for orthomosaic construction in Agisoft Metashape .....	75
Table 18: Plots used as ground control points .....	77
Table 19: Parameters for error reduction in Agisoft Metashape.....	77
Table 20: Parameters for PCA in ENVI .....	79
Table 21: Accuracy assessment for SVM with band means, category 1 .....	83
Table 22: Accuracy assessment for SVM with band means, category 2 .....	84

Table 23: Accuracy assessment for SVM with band means, category 3 .....	84
Table 24: Accuracy assessment for SVM with band means and sd, category 3 .....	85
Table 25: Accuracy assessment for SVM with band means, category 4 .....	85
Table 26: Accuracy assessment for SVM with NDRE mean and sd, category 1 .....	86
Table 27: Accuracy assessment for SVM with NDRE mean and sd, category 2 .....	86
Table 28: Accuracy assessment for SVM with NDRE mean, category 3 .....	87
Table 29: Accuracy assessment for SVM with NDRE mean and sd, category 3 .....	87
Table 30: Accuracy assessment for SVM with NDRE mean and sd, category 4 .....	88
Table 31: Accuracy assessment for SVM with NDVI mean and sd, category 1 .....	88
Table 32: Accuracy assessment for SVM with NDVI mean and sd, category 2 .....	89
Table 33: Accuracy assessment for SVM with NDVI mean, category 3 .....	89
Table 34: Accuracy assessment for SVM with NDVI mean and sd, category 3 .....	90
Table 35: Accuracy assessment for SVM with NDVI mean and sd, category 4 .....	90
Table 36: Accuracy assessment for SVM with PCA means, category 1 .....	91
Table 37: Accuracy assessment for SVM with PCA means, category 2 .....	91
Table 38: Accuracy assessment for SVM with PCA means, category 3 .....	92
Table 39: Accuracy assessment for SVM with PCA means and sd, category 3 .....	92
Table 40: Accuracy assessment for SVM with PCA means, category 4 .....	93
Table 41: Sentra 6X and Parrot Sequoia band specifications .....	94
Table 42: Comparison between Sentra 6X, Parrot Sequoia, and Micasense Dual Camera .....	95
Table 43: PCA loadings for Sentra 6X .....	96
Table 44: PCA loadings for Parrot Sequoia .....	96
Table 45: Regression models predicting eelgrass cover from various cameras .....	97

## 1.0 | Introduction

### 1.1 | Eelgrass in the Pacific Northwest

Eelgrass provides a variety of critically important ecosystem services in nearshore marine environments in the Pacific Northwest. These services include the provision of habitat for Dungeness crabs (*Cancer magister*) and juvenile salmon (*Oncorhynchus* spp.) as well as moderating storm surge (Barbier et al. 2011, Rubin et al. 2018). Two species of eelgrass occur in the Pacific Northwest: the native *Zostera marina* and the introduced *Zostera japonica*. *Z. japonica* was introduced to the Pacific Northwest in the early 1900's, likely as a contaminant of the Japanese oyster cultivation in Willapa Bay and northern Puget Sound (Harrison and Bigley 1982). *Z. japonica* typically grows higher in the intertidal zone and has proliferated in naturally unvegetated areas of the tidal flats above the elevation of *Z. marina* (Baldwin and Lovvorn 1994, Hahn 2003, Ruesink et al. 2010). Over the course of a year, growth patterns for both eelgrass species fluctuates seasonally. Maximum biomass for *Z. japonica* and *Z. marina* in Padilla Bay, Washington peaks between June and August (Thom 1990). The shoot density of *Z. japonica* declines dramatically in the fall, with an annual minimum of less than 100 shoots m<sup>-2</sup> in January, followed by a dramatic increase in the spring, with an annual maximum of over 3,200 shoots m<sup>-2</sup> in July (Thom 1990). The shoot density of *Z. marina* stayed relatively consistent over the year at around 500 shoots m<sup>-2</sup>, but with seasonal variation in biomass in response to changes in leaf area/shoot length (Thom 1990).

Almasi and Eldridge (2008) modeled the *Z. japonica* in the Yaquina estuary on the Oregon coast and found that most important limiting factors to growth were limited vegetative shoot and seedling survival. In the same estuary, Young et al. (2015) recorded a 1500% increase in the areal extent of *Z. japonica* from 1997 to 2007 but did not observe a related decrease in *Z.*

*marina* extent during that time. This indicates that *Z. japonica* is capable of proliferating in areas without competition with *Z. marina*. Under simulated summer conditions, Harrison (1982) observed that when submerged, *Z. marina* grew more than twice as fast as *Z. japonica*, potentially shading *Z. japonica* and limiting its ability to spread into *Z. marina* vegetated areas. Since it grows at higher elevations, *Z. japonica* is more frequently exposed at low tides and for longer periods of time than *Z. marina*. In part of its invaded range, *Z. japonica* grows better under higher temperatures, making it more resistant to extremes in environmental conditions (Shafer et al. 2008, Ruesink et al. 2010).

Interactions between *Z. marina* and *Z. japonica* have been increasingly studied in the Pacific Northwest as *Z. japonica* expands its range. In a transplant experiment in Willapa Bay, Bando (2006) found that interspecific competition between *Z. japonica* and *Z. marina* reduced above-ground biomass more than intraspecific competition. Furthermore, Bando (2006) disturbed the transplanted plots by removing the plants and recording the natural revegetation patterns over the following two years. This disturbance was meant to mirror common disturbances to mudflats, such as shellfish dredging and trampling. They found that disturbance increased productivity and fitness in *Z. japonica* but decreased productivity and fitness in *Z. marina* (Bando 2006). In Willapa Bay, the removal of *Z. japonica* has also been found to positively affect the growth of *Ruppia maritima*, suggesting that *Z. japonica* outcompetes species outside the family Zosteraceae (Boardman and Ruesink 2022).

Competition between *Z. marina* and *Z. japonica* is exhibited on a microtopological level as well. Hannam and Wylie-Echeverria (2015) conducted several transplant experiments in Padilla Bay which showed *Z. marina* suppressed *Z. japonica* above-ground biomass by over 60% in pools and 47% on mounds. However, due to its physiological limits, *Z. marina* was less

prevalent on mounds regardless of *Z. japonica* presence (Hannam and Wylie-Echeverria 2015). Thus, *Z. marina* excludes *Z. japonica* from areas where it is well-established and has adequate water cover, whereas *Z. japonica* can establish itself in the higher intertidal where *Z. marina* can neither thrive nor compete.

Epiphytes colonize eelgrass leaves shortly after they emerge and have been recorded to consist of 11% of annual biomass and 50% of above-ground net primary production (NPP) in Padilla Bay (Thom 1990). In Netarts Bay, Oregon, differing quantities of epiphytic diatom species on *Z. marina* were recorded seasonally, with one group dominant from November to July (species of *Cocconeis*, *Gomphonema*, *Rhicosphenia*, *Synedra*, and *Navicula directa*), and another from August to October (species of *Navicula* and *Nitzschia*) (Whiting 1983). In Padilla Bay, eelgrass epiphytes have also been found to vary seasonally, and have their peak biomass in June (Thom 1990). The dominant epiphytes observed during the June biomass peak in Padilla Bay were diatoms, *Ceramium pacificum* (red alga), and *Ulva fenestrata* (green alga) (Thom 1990). Thom (1990) also noted that *C. pacificum*, *U. fenestrata*, and *Gracilaria pacifica* were most common in the *Z. marina* beds. Epiphytes are thought to hinder eelgrass growth by restricting light exposure to the eelgrass leaves. The abundance of grazers can impact epiphyte biomass, and in turn, limit the potential adverse effects of epiphytes on eelgrass growth. For example, the isopod, *Idotea resedata* reduced epiphyte biomass by one-third in Padilla Bay (Williams and Ruckelshaus 1993).

## 1.2 | Ground monitoring efforts

The extent of eelgrass in Puget Sound has been monitored by coastal managers in a variety of ways. Ground-based methods, such as using transects and quadrats to mark sampling areas, provide a detailed picture of many eelgrass characteristics. This method can

cover from the upper intertidal to the subtidal using divers. Furthermore, ground-based methods have been used for many years, which allows for easily repeatable change analyses over long periods of time. The Nearshore Habitat Program at the Washington DNR employs the use of towed underwater videography in their Submerged Vegetation Monitoring Program (SVMP) to survey subtidal and intertidal *Z. marina* beds in many Puget Sound eelgrass communities. This method is less intensive than diver transects and can still cover subtidal *Z. marina* beds. In some cases, plant characteristics are not as easily identifiable as in ground-based methods. Berry et al. (2003) noted that only catastrophic changes in some *Z. marina* characteristics were detectable using this method. Also, current SVMP observations do not include the upper intertidal areas where *Z. japonica* is found, and thus lack *Z. japonica* area estimates (Christiaen et al. 2016). Padilla Bay, Washington contains over 3000 ha of eelgrass in one of the largest contiguous beds in North America (Bulthuis 1995). According to ground monitoring data and aerial photos taken of the boundary between vegetated and unvegetated areas, *Z. japonica* area in Padilla Bay increased from 236 ha in 1989 to 669 ha in 2004 (Bulthuis and Shull 2006).

### 1.3 | Remote sensing for seagrass monitoring

Satellite imagery and crewed flights are frequently used to monitor eelgrass. Both methods employ multispectral imagery which is useful for vegetation monitoring. In Padilla Bay alone, eelgrass has been mapped using satellite imagery, standard aerial color photography, and compact airborne spectral imagery (Webber et al. 1987, Bulthuis 1995, Shull 2000). Satellite imagery has been used for large area coverage and the regular revisit times and the long time series of available imagery (since 1972 for Landsat) makes this approach an attractive method for monitoring environmental change (Klema 2015). However, satellite resolution is



generally quite low (~10s of meters), with the exception of new satellites such as Worldview 4 which provides multispectral imagery with a resolution of 1.24 m. Yet, the inability to coordinate satellite image acquisition with low tide events makes it challenging to monitor interannual changes using this imagery in nearshore marine environments.

Crewed flights are more flexible than satellite imagery with regard to timing data collection with low tide events. Bulthuis (1995) and Shull (2000) timed manned flights to coincide with the lowest tide of the year. Ball et al. (2014) used aerial imagery obtained from 43 crewed flights from 1939 to 2011 to calculate changes in seagrass area. These images were orthorectified to 0.3 m per pixel resolution. They compared the efficacy of unsupervised classification methods to delineate seagrass extent, including the use of a principal component analysis (PCA) to inform classification (Ball et al. 2014). While crewed flights offer a relatively high-resolution option for a large area, costs are often prohibitive and may not be realistic to repeat multiple times within a single growing season.

Small uncrewed aerial systems (UAS) may provide an efficient way to acquire data for environmental research and monitoring with both high temporal and spatial resolution that will complement current ground-based, satellite, and crewed aircraft methods (Anderson and Gaston 2013). The growing recreational and commercial market for UAS has driven the costs down dramatically and has led to greatly increased capability. The low cost, the very high spatial resolution (10 cm or better), and the ability to precisely time flights during low tide events and days with low wind speeds and sun angles are attractive features of this technology (Bryson et al. 2013, Casella et al. 2017). Some modern multispectral sensors that can be mounted on UAS have more bands than most satellites and may be the key to unlocking spectral differences between vegetation types. In automated, unsupervised classification approaches, having multiple narrow

bands in each region of the visible spectrum provides more information upon which to base the classifications. For example, the “red edge” region of the spectrum, which is between the red and near infrared, has long been purported as a region of importance for estimating chlorophyll content (Gates et al. 1965). The Micasense Dual Camera Imaging System is a cutting edge 10-band multispectral camera which contains three bands in the red edge region of the spectrum (Micasense). In theory, having these additional bands will help elucidate the variations in spectral signatures due to differences in chlorophyll content.

Nahirnick et al. (2020) used historical aerial imagery alongside UAS imagery to conduct an eelgrass change detection study in the Salish Sea or British Columbia. They visually interpreted eelgrass extents for both sets of imagery and evaluated change in area and shape in accordance with environmental indicators such as shoreline activities and residential housing density. Nahirnick et al. (2020) found that human activities were strongly correlated with both decreased eelgrass area and increased meadow fragmentation. From 1932 to 2016, eelgrass area at their study sites on Mayne and Saturna islands decreased by an average of 45.1%, highlighting the importance of monitoring eelgrass extent in the Salish Sea (Nahirnick et al. 2020). However, visually estimating eelgrass extents is time-consuming and introduces user error. In this study, I will investigate unsupervised segmentation techniques that rely on spectral data for delineation alongside supervised classification of eelgrass cover. For an environment in which sampling time is limited by tidal events, UAS flights have the potential to be the accurate, low impact (e.g., no trampling of eelgrass) method needed to detect small-scale change in eelgrass meadows.

#### 1.4 | Research goals

The objective of my study is to obtain high-resolution, multispectral imagery over the course of the 2020 growing season of the PB-NERR transects in Padilla Bay, Washington using

a UAS. I will use this imagery to build predictive models of percent cover of both *Z. marina* and *Z. japonica* in 2020. Due to the fluctuations in epiphyte load throughout the year for *Z. japonica* and *Z. marina*, I will also determine whether there are significant differences in epiphyte load from June to September and determine whether there are also species-specific differences in epiphyte load.

## 2.0 | Methods

### 2.1 | Study area

This study was conducted in Padilla Bay, in Skagit County, Washington. Padilla Bay contains more than 3,000 hectares of eelgrass and is contained by the mainland to the east, Samish Island to the north, Guemes Island to the west, and Fidalgo Island to the south and west (Figure 1, Bulthuis 1995).

Three permanent monitoring transects established and supervised by the Padilla Bay National Estuarine Research Reserve (PB-NERR) exist in the northern section of the bay (Figure 1). These transects extend over 4 km from shore and are divided into 6 zones (Table 1). The study area transitions from unvegetated mudflats to *Z. japonica* dominated meadows, then to *Z. marina* dominated extents in the lower intertidal and subtidal regions of the transects (Table 1).

Table 1. Padilla Bay National Estuarine Research Reserve permanent monitoring zone characteristics and distance from shore.

Zone	Approximate distance from shore (m)	Characteristics
1	0-300	Unvegetated, intertidal
2	300-800	<i>Z. japonica</i> dominant, intertidal
3	800-1485	Mix of <i>Z. japonica</i> and <i>Z. marina</i> , with <i>Z. japonica</i> dominant, intertidal
4	1485-1915	Mix of <i>Z. japonica</i> and <i>Z. marina</i> , with <i>Z. marina</i> dominant, intertidal
5	1915-3490	<i>Z. marina</i> dominant, intertidal
6	3490-4385	<i>Z. marina</i> dominant, subtidal

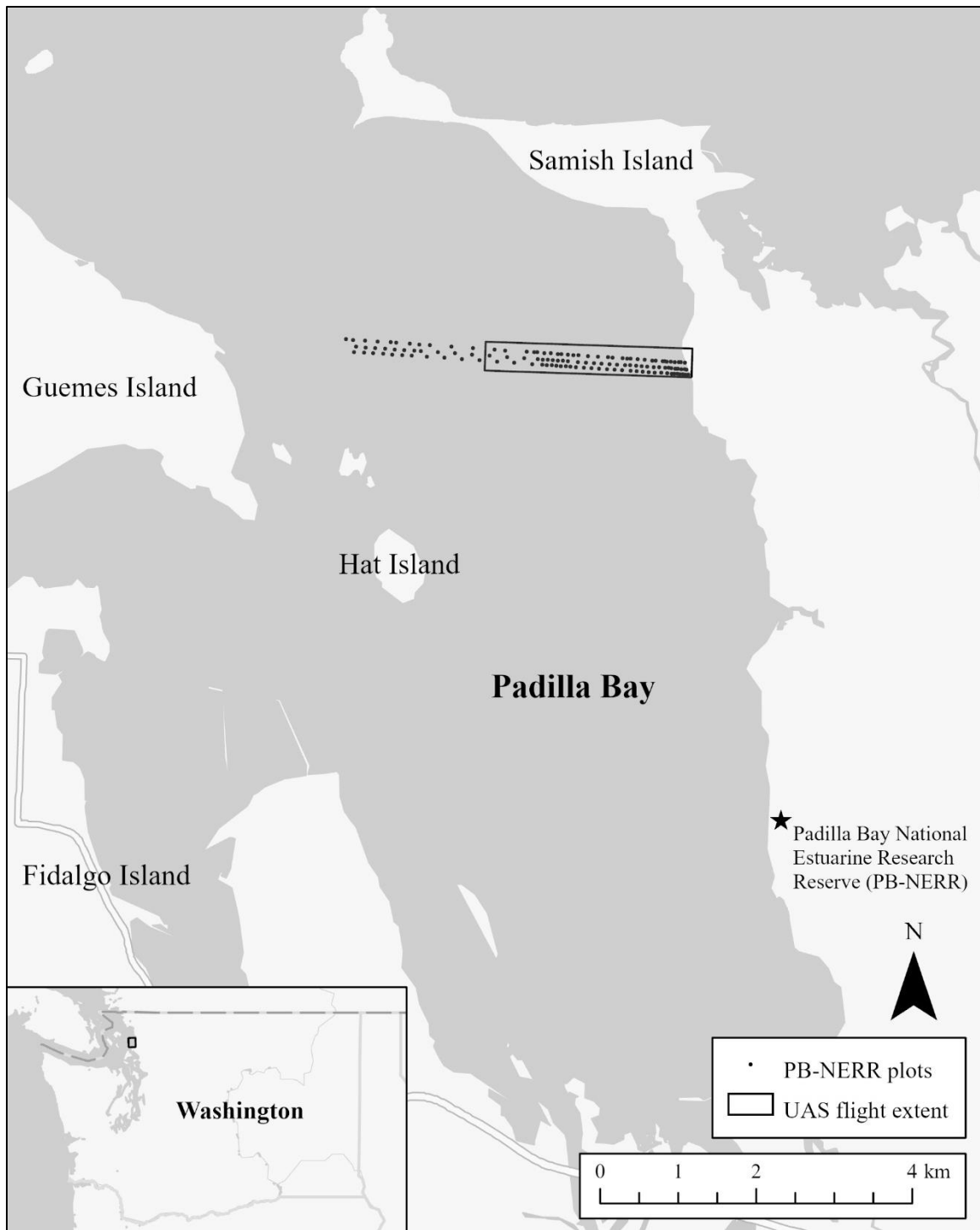


Figure 1. Overview of the study site at Padilla Bay, Washington. Permanent biomonitoring plots spread across 3 transects maintained by PB-NERR extend approximately 4 km into Padilla Bay. For the purposes of this study, I surveyed plots in the first 2.5 km of the transects. Map data are from PB-NERR, Esri, HERE, Garmin, FAO, NOAA, and USGS.

For the purposes of this study, I fully covered zones 1-4 and flew over a portion of zone 5. I did not include any of zone 6 in the flight path since the eelgrass would not be exposed at low tide. Also, PB-NERR researchers monitor zone 6 using divers which was outside the scope of ground truth data collection for this study.

## 2.2 | Permanent monitoring plots

Within each of the three transects, there are seven permanent plots in each of the six zones, for a total of 126 plots (Figure 2). The transects are 4 km long, oriented on an east-west axis. The transects are spaced approximately 75 m apart north to south. The zones are determined by the dominant cover type (Table 1). Within each zone, seven permanent plots are distributed evenly across the length of the zone, ranging from only 50 m apart in Zone 1, to 275 m apart in Zone 5. Each plot has a PVC marker along the transect marking the general location of the plot. Each PB-NERR monitored plot is located 2 m directly north of the PVC marker and is 0.5 x 2 m in area orientated east-west along the 2 m axis. The corners of the plot are marked with short pins in the sediment. All 126 of the PVC markers have GPS coordinates, and 53 have highly accurate RTK coordinates. Markers placed on a subset of these 53 locations just prior to the UAS flights were used to georectify the orthomosaics in the image processing steps.

## 2.3 | UAS flights

### 2.3.1 | Equipment

I used a DJI Matrice 210 UAS mounted with a Micasense Dual Camera Imaging System to conduct all flights. The Micasense camera has 10 bands, and the distribution of these bands provides coverage in the visible spectrum as well as the transition to the infrared part of the spectrum (Table 2). The Micasense camera system bands are comparable to those of widely

used satellites such as Landsat 8 and Worldview 2 (Figure 3). The sensor resolution is 1280 x 960 pixels (Micasense).

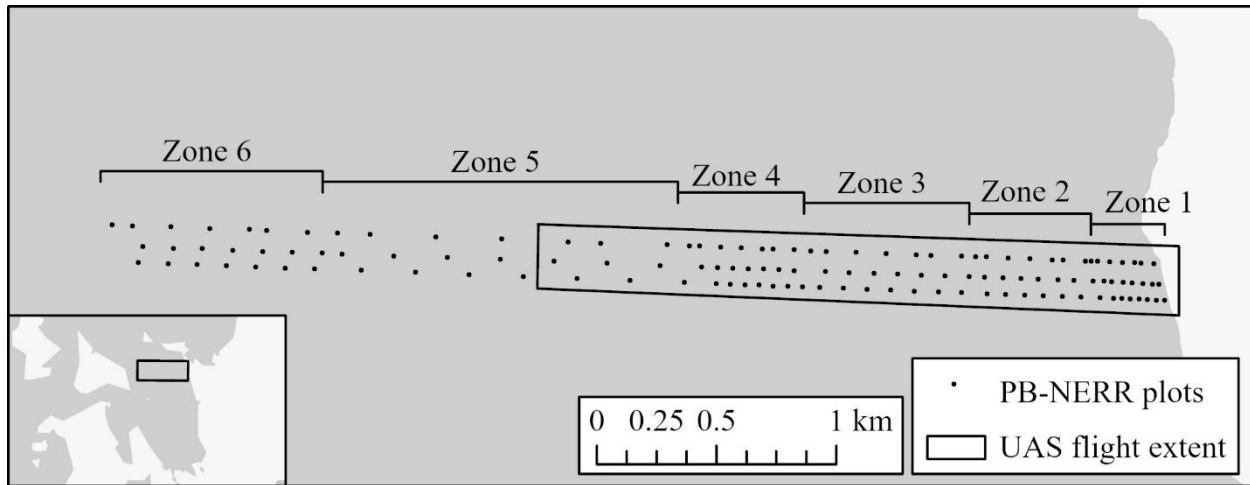


Figure 2. Map of permanent plots used for annual monitoring by PB-NERR showing the zone divisions and the UAS flight extent.

Table 2. Micasense Dual Camera Imaging System spectral band specifications. In the following sections, bands will be written as: name-center wavelength(band range). For example: Coastal blue 444(28).

<b>Band Number and Name</b>	<b>Center Wavelength (nm)</b>	<b>Band Range (nm)</b>
1- Coastal blue	444	28
2- Blue	475	32
3- Green	531	14
4- Green	560	27
5- Red	650	16
6- Red	668	14
7- Red edge	705	10
8- Red edge	717	12
9- Red edge	740	18
10- Near infrared	842	57

### 2.3.2 | Flight path development

Flight path polygons were developed in the DJI Pilot App. The polygon used for all flights was 225 m north to south and 2,500 m east to west. This ensured that there would be a buffer to the north and south of the transects so the plots used for ground truth data would be captured in the imagery. The polygon was adjusted so there would be 6 flight lines out and 6 flight lines back to cover the study area, allowing for plenty of battery life in case of emergency. The side overlap was set to 75% and the frontal overlap was set to 80%. The same flight polygon was used for all flights, ensuring the same area was captured for all flight dates (Figure 1). The flight altitude was 90 m resulting in a ground resolution of 6 cm. Given these parameters, each flight could be completed in about 90 minutes, including two brief stops to change batteries.

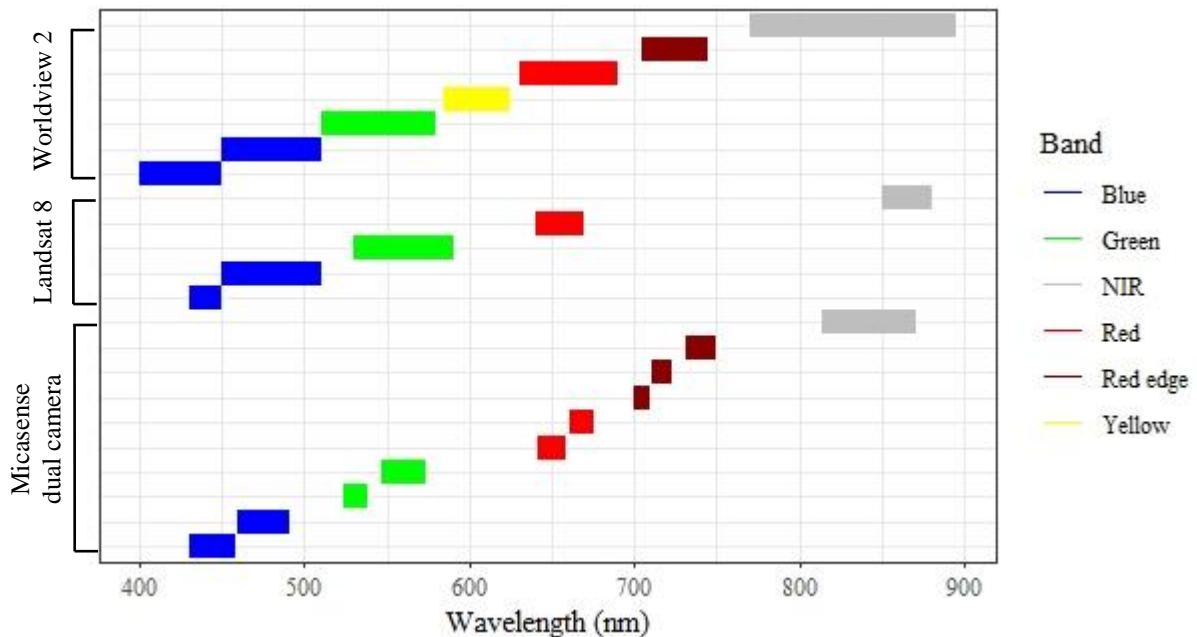


Figure 3. Comparison of Micasense Dual Camera Imaging System, Landsat 8, and Worldview 2 spectral bands. At our flight altitude of 90 m above ground level, the Micasense Dual Camera Imaging System has a spatial resolution of 6 cm per pixel. The Landsat 8 satellite has a spatial resolution of 30 m for each of the five bands displayed. The Worldview 4 satellite has a spatial resolution of 1.24 m.



### 2.3.3 | Scheduling flights

To get the best quality imagery possible, I scheduled flights around the lowest low tides when the eelgrass was the most exposed. Using a combination of tide charts and PB-NERR scientist experience of tidal patterns in Padilla Bay, I planned 8 flight dates during the summer of 2020. Unfortunately, I had to cancel the September 15 flight due to wildfire smoke and extremely low visibility. To determine the start time for each flight, I first calculated the time of the lowest low tide at the study site. According to PB-NERR researchers, the transect area typically reached the lowest low tide approximately 50 minutes after the predicted low tide at the Swinomish Channel tide station which is located 17 km south of the study area (NOAA Tides & Currents 2020). I planned to start each flight 90 minutes before the low tide at the study site to ensure all imagery would be captured before the tide changed direction. This was done help keep the imagery consistent since the grass blades would flow in the direction of the ebb current. The average tide stage during the flights was -2.1 ft.

### 2.3.4 | Flight protocol

On the day of the flight, two field volunteers were given 0.5 by 0.5 m panels with a “checkerboard” pattern to place over 33 of the PVC pipes with high-resolution RTK coordinates. These panels served as ground control during the image processing and were all within the first 5 zones of transects 1 and 3 (Table 18). After placing the last ground control panel, volunteers walked back to a position that was about 2000 m from shore. The volunteers carried radios to facilitate contact with the flight crew who operated from the beach at the east end of the transect. Between the volunteers and the flight crew on shore, we were able to maintain visual line of sight of the UAV during all phases of the flight. After the flight, ground control panels were collected and returned to shore.

Prior to starting the flight, and at each battery change during a flight, I captured an image of the Micasense Calibrated Reflectance Panel. This calibration panel has a known, wavelength-specific reflectance. During post-processing, use of these calibration images enables me to convert the brightness index values in each image to reflectance values and therefore controls for variation in solar illumination (due to sun angle, clouds, and aerosols) both within and between flights. This step ensures that imagery taken on different dates are comparable.

Using the DJI Pilot app, I loaded the pre-planned flight path to the UAV. I manually operated the UAV to takeoff and fly to the starting altitude. Once the UAV was near the starting point for the flight path, I switched from manual to autopilot and the UAV started the data collection. Each flight consisted of at least 3 segments, with each segment typically consisting of 2 flight lines out and 2 flight lines back. Each segment typically lasted between 21 and 23 minutes and covered 10 km of image collection. Near the end of the battery life of each segment, I landed the UAV on shore, changed the batteries, and took another photo of the calibration panel. I then took off manually and resumed the programmed flight. All flights were conducted in accordance with the Federal Aviation Administration (FAA) Part 107 regulations (FAA 2020).

## 2.4 | Biological sampling

### 2.4.1 | Plot selection

I randomly selected 28 plots from the 126 PB-NERR monitoring plots at which to collect ground truth data throughout the field season. These data were intended to supplement the data for all 126 plots that were collected by PB-NERR staff on July 4 and July 5, 2020. I stratified the random selection by zone since each zone is characterized by different dominant cover types. I excluded zone 1 from the selection because it is unvegetated. I excluded zone 6 because it is subtidal and was out of range for the flights. While I kept the original plot names used by PB-

NERR, I did not sample in the exact location of their permanent plots to avoid disturbing their annual data collection. Instead, I set up temporary plots south of the PVC marker for my ground truth collection dates.

#### 2.4.2 | Percent cover

Percent cover was recorded at the 28 plots in July, August, and September. I built a 0.5 m by 2 m plot, consistent with those used in the annual PB-NERR biomonitoring. I oriented each plot E-W along its 2 m axis. The northeast corner of the plot was positioned 2, 3, or 4 m due south of the PVC marker in July, August, and September, respectively. This was done so that the eelgrass would not be disturbed by footprints made to access the study area, nor would eelgrass plant collection impact future percent cover observations.

I used a point intercept method to record percent cover. I built a 0.5 m by 0.5 m plot with string crossing at 5, 15, 25, 35, and 45 cm on both axes to form a grid with 25 string intersections. I recorded the topmost cover type at each of the 25 intersections. Cover type was marked as algae (primarily *Ulva* sp.), bare, detritus (primarily dead eelgrass), live *Z. japonica*, or live *Z. marina*. This process was conducted four times, totaling the length of the 0.5 x 2 m plot.

#### 2.4.3 | Epiphyte measurements

I anticipated that epiphytes may alter the spectral signature of the eelgrass and, since epiphyte mass is known to vary seasonally in Padilla Bay, this could be a source of noise in my analysis (Thom 1990). To assess seasonal variation in epiphyte load, one plant was collected at each plot for both *Z. marina* and *Z. japonica*. The plant was selected from the northeast corner of the plot. If no plant of that species was present in the northeast corner, the rest of the plot was searched. Eelgrass sample collection was abandoned if there was no plant of that species

available within the vicinity of the plot. Since eelgrass samples were collected after image collection, taking a sample did not impact the percent cover measured. Plants were clipped at ground level to exclude below-ground mass. Before placing samples in collection bags, I removed sediment and epifauna such as snails and isopods. Samples were placed into individual Ziploc bags and labeled with the plot, plant species, and date.

In the lab, I measured and recorded the shoot length from the base of the clipping to the end of the longest leaf. Then, I used a razor blade to carefully scrape the epiphytes off each blade of grass. The epiphytes scraped from each sample were collected onto individual coffee filters labeled with the collection date, plot, and the species of the eelgrass sample. The clean eelgrass sample was placed into an individual paper bag and labeled according to plot, species, and date.

I dried the bags containing eelgrass biomass and coffee filters containing epiphyte biomass in a drying oven at 70° C for 48 hours. I used an analytic balance for all mass measurements. To take the eelgrass biomass, I took the dried sample out of the paper bag used for drying and placed the sample on the balance tray. Since it was impossible to remove the dried epiphytes from the coffee filters, I put the entire filter including the epiphytes in the tray and recorded the mass. To account for the mass of the clean filter, I placed 5 clean filters in the drying oven and recorded the mass of each dried filter. To determine epiphyte biomass, I subtracted the average dried filter mass from the overall filter and epiphyte mass.

## 2.5 | Image processing

Each flight generated over 23,000 individual images with a separate set of images for each of the ten bands. I processed this imagery using Agisoft Metashape Professional Version 1.6.4 build 10928 (64 bit). The workflow was largely based on instructions published by the United States Geological Survey National Unmanned Aircraft Systems (UAS) Project Office and

the Agisoft Helpdesk Portal (USGS National UAS Project Office 2017). A detailed method outlining the workflow used to create various GIS layers from the imagery collected with the DJI Matrice 210 and Micasense Dual Camera System can be found in the appendix.

For each date, the result was a ten band orthomosaic with a ground resolution of 6 cm. Additional processing was conducted using ENVI 5.6 + IDL 8.8 (64-bit) software. The first step simply involved resampling the imagery to a ground resolution of 10 cm. This was done to somewhat reduce the data volume and because this resolution was deemed to be adequate for my analysis and 10 cm pixel were better suited to extracting spectral data from the 0.5 by 2.0 m ground truth plots. The next step involved converting the raw image data from digital numbers (integer values ranging from 0 to 32768 that are simply a reflectance index) to actual reflectance values ranging from 0 to 1. I did so using the following formula for each of the 10 bands:

$$= (DN \text{ band } x) / 32768$$

## 2.6 | Calculation of PCA, NDVI, and NDRE

In ENVI, I ran a PCA with all 10 Micasense bands with the goal of reducing the dimensionality of the dataset while retaining much of the variation in the data. Khan et al. (1992) found using a PCA in coastal habitats to be useful in reducing the effect of water depth on multispectral imagery. Similarly, Ball et al. (2014) found classification based on PCA results to accurately differentiate seagrass habitat. The parameters used in ENVI to conduct the PCA are provided in the appendix (Table 20). I retained the first three PC layers to use as predictor variables. I also interpreted the contrasts present in the loadings of the PCA and how they varied throughout the first three PCs.

I also generated Normalized Difference Vegetation Index (NDVI) and Normalized Difference Red Edge Index (NDRE) layers in ArcGIS Pro. These metrics are commonly used as

vegetation health indices (Campbell 2007). I calculated two different versions of NDVI using both red bands from the Micasense camera (Table 2) in the following equation:

$$NDVI = (NIR - Red) / (NIR + Red)$$

I also calculated three versions of NDRE using each of the three red edge bands from the Micasense camera (Table 2) in the following equation:

$$NDRE = (NIR - Red\ edge) / (NIR - Red\ edge)$$

Each of the normalized difference indices will be referred to with a subscript that refers to the band numbers in Table 2. For example,  $NDVI_{6,10}$  refers to the NDVI calculated with bands 6 and 10. Following these steps, I had 18 data layers (the eight layers described above plus the reflectance values for the original 10 bands) from which to extract plot-level values.

## 2.7 | Object-based image analysis

Image segmentation was conducted in eCognition Developer 10.2 (Trimble Germany GmbH 2021). My workflow for developing image segments was largely informed by video tutorials produced by eCognition Developer (2019). I imported a full season mosaic (all flight dates) of the imagery into eCognition. This layer contained all 10 bands from the Micasense camera. Prior to segmenting the image, I calculated two NDVI layers, one each for the two red bands of the Micasense camera. Upon visual inspection, I decided that the NDVI calculated with the red 668(14) band was better at delineating between bare and vegetated areas and I used this layer to mask out unvegetated areas prior to segmenting the rest of the image mosaic.

To segment the vegetated area, I used the multi-resolution segmentation tool. This method allows for multiple data layers to inform the segmentation and depends on the desired scale, shape, and compactness of the resulting segments. Multi-resolution segmentation is

commonly used in scenarios where spectral data are the primary data source for segmentation (as opposed to existing feature classes such as building outlines, municipal boundaries, etc.) and has previously been used for grassland classification (Xu et al. 2019). Scale, shape, and compactness parameters of 100, 0.1, and 0.5, respectively, were used to segment the imagery. A scale parameter of 100 sets the minimum object size as 100 pixels, which equals 1 m<sup>2</sup> for this study. The shape parameter is chosen in accordance with how much emphasis should be placed on shape versus color. Since this study is interested in the spectral qualities of vegetation, I set the shape parameter to 0.1. Finally, the compactness parameter was set to 0.5 to place an even emphasis on compactness versus smoothness in the resulting image shapes. I used different source data to create four versions of the segmentation: one with the 10 Micasense bands, one with the 3 principal components, one with the NDVI<sub>6,10</sub> layer, and one with the NDRE<sub>7,10</sub> layer. Summary statistics for the segments in each of these versions were exported to Microsoft Excel.

## 2.8 | Statistical analysis

Statistical analysis was performed in RStudio Version 1.3.1093 (RStudio Team 2020). Raw band reflectance, vegetation indices, and PCA values were used to build linear models to predict percent cover of *Z. marina*, percent cover of *Z. japonica*, and total percent cover of eelgrass (combined *Z. marina* and *Z. japonica*) (Table 3).

Table 3. List of plot-level variables used in statistical models to predict percent cover of *Z. marina*, *Z. japonica*, and total *Zostera* spp. cover. Predictor variable values were obtained by taking the mean value for each plot.

Variable	Data source
Response variables:	
Total <i>Zostera</i> spp. % cover	Field observations by Hein, July-September 2020
<i>Z. marina</i> % cover	Field observations by Hein, July-September 2020
<i>Z. japonica</i> % cover	Field observations by Hein, July-September 2020
Total <i>Zostera</i> spp. % cover	Field observations by PB-NERR, July 2020
<i>Z. marina</i> % cover	Field observations by PB-NERR, July 2020
<i>Z. japonica</i> % cover	Field observations by PB-NERR, July 2020
Predictor variables:	
Bands 1-10	Raw data collected by the Micasense camera
NDRE <sub>7,10</sub> , NDRE <sub>8,10</sub> , NDRE <sub>9,10</sub>	NIR band 10 and red edge bands 7, 8, and 9
NDVI <sub>5,10</sub> , NDVI <sub>6,10</sub>	NIR band 10 and red bands 5 and 6
Principal components 1-3	PCA calculated from 2020 spectral data

To extract these values for the pixel-based analysis, I used ArcGIS Pro 2.6.0 to create a polygon feature layer where polygons represented the location of the 126 ground truth plots sampled by PB-NERR personnel and the 28 ground truth plots that I sampled. Coordinate data for the plots were calculated relative to the GPS coordinates for the PVC markers that were provided by PB-NERR. For each ground truth plot, I used ArcGIS Pro to extract and export data from the layers representing each of the predictor variables. For each plot, I calculated the mean for each predictor variable. These values were exported to and compiled in Microsoft Excel. This process was conducted for each of the 10 bands, as well as for the PCA layers calculated in ENVI and NDVI and NDRE layers calculated in ArcGIS Pro. I will compare the predictive power of the PCA to that of NDVI, NDRE and raw reflectance values for each of the 10 bands.

To extract values for the object-based image analysis, I identified the image segments which contained the ground truth plots for each of the four segmentations (band, PCA, NDVI,



NDRE). The mean reflectance and standard deviation of each segment were joined with the associated ground truth plot. These summary statistics were exported to Microsoft Excel and used as training and test data. I used these values to build categorical Support Vector Machine (SVM) models in the “e1071” package in R to classify the segments based on percent cover of *Z. japonica* and *Z. marina* (Meyer et al. 2021). I used k-fold cross validation to evaluate the classification and used confusion matrices to determine overall, user’s, and producer’s accuracy.

### 3.0 | Results

#### 3.1 | Image quality

I successfully completed 8 image collection flights between June 7 and August 29, 2020. Using Agisoft Metashape, I was able to generate orthomosaics for six of these images (Figure 12-17). For the August 18 flight, imagery from a small portion of the eastern section of the transect could not be stitched together (Figure 17). This section was mostly featureless bare mud. I was unable to generate orthomosaics for the low sun angle flight from June 24 due to the high tide stage and the flight from August 29 due to the high tide, wind, and waves.

##### 3.1.1 | Sun glint

The presence of sun glint proved to be a challenge in capturing reliable, good quality imagery of the study area. Imagery collected during the June 7 and June 23 flights was heavily impacted by sun glint. Upon initial visual inspection of the orthomosaics, there were areas of reflectance distortion due to sun glint. This is a common problem in UAS imagery captured over bodies of water. Nahirnick et al. (2019) suggest flying with sun angles lower than  $40^\circ$ , cloud cover less than 10% or more than 90%, and wind speeds less than  $5 \text{ m s}^{-1}$  would limit sun glint. In scheduling flights, I prioritized the lowest tides over sun angle primarily because Nahirnick et al. (2019) worked in areas with submerged eelgrass and their main goal was to delineate the eelgrass extent, not to predict biological characteristics (e.g., percent cover or species delineation) from the spectral signatures in the imagery. However, I did take these guidelines into consideration and planned the flight for the lowest sun angle possible given the lowest tide stage. Variable wind speeds and a changing sun angle over the course of a single day of imagery collection impacted the image quality. For example, on the July 4, 2020 collection date, the sun

angle increased from 50.1° to 61.2° during the 90-minute flight period. As a result, images taken later in the flight when the sun angle was higher contain more sun glint.

To investigate how much the sun glint was impacting the overall imagery, I exported the reflectance histograms for each band for each of the imagery collection dates. Based on these histograms, it was evident that the upper limits of the reflectance were different depending on the band. For example, since the study area is primarily vegetated, reflectance values in the NIR band were higher than those in the blue band. If I were to impose the same upper threshold of reflectance to represent sun glint on all the bands, it would result in masking out values on some bands that naturally have higher reflectance, even with the absence of sun glint.

Upon visual inspection of the imagery, I determined that approximately 5% of the area of the total imagery from the 2020 field season consisted of sun glint. I used the image statistics to identify the threshold representing the 95<sup>th</sup> percentile of total reflectance for each band. I created a binary mask where pixels above the 95<sup>th</sup> percentile value were given a value of 0 and pixels below the 95<sup>th</sup> percentile were given a value of 1. I repeated this process for all 10 bands in the full season mosaic of imagery. In some cases, the pixels identified as sun glint varied in location depending on the band. To avoid a situation in which a pixel has values for some bands, but not all, I multiplied the 10 binary masks together. This resulted in one binary mask per imagery date in which all pixels identified as sun glint for any band were given a value of 0. Finally, I multiplied this mask by the orthomosaic image of that date to create an orthomosaic where the sun glint pixels have a value of 0 which I set as the “No Data Value”.

After filtering out the sun glint pixels, the June 7 and June 23 orthomosaics were left with swaths of “no data” on the southern edge of the study area and in several streaks across the middle of the transects (Figure 12, Figure 13). Imagery from July 4 and July 21 was moderately

impacted by sun glint in the southern part of the transects but was unaffected in the northern half of the transects (Figure 14, Figure 15). The best quality imagery in terms of sun glint was captured on August 1 and August 18, 2020. Streaking is minimal throughout the August orthomosaics, and few pixels needed to be removed in the sun glint filtering process (Figure 16, Figure 17). Since the June 7 and June 23 imagery was highly impacted by sun glint and filtering removed many pixels, I decided not to use those orthomosaics for analysis (Table 4). I cropped the July 4 and July 21 orthomosaics so that they contained only the northern half of the orthomosaic (Table 4). Thus, for analysis of these dates, only transect 1 ground truth plots are considered. Finally, I used the entire orthomosaic for each the August 1 and August 18 flights since they were minimally impacted by sun glint (Table 4).

Table 4. Summary of imagery used in final analysis for the “full season” dataset.

<b>Date</b>	<b>Portion of orthomosaic used in final analysis</b>	<b>Reason for exclusion</b>
6/7/20	Not used	Full scene severely impacted by sun glint
6/23/20	Not used	Full scene severely impacted by sun glint
6/24/20	Not used	Orthomosaic did not stitch together due to high tide
7/4/20	Transect 1 only	Transects 2 and 3 impacted by sun glint
7/21/20	Transect 1 only	Transects 2 and 3 impacted by sun glint
8/1/20	Full scene	N/A
8/18/20	Full scene	N/A
8/29/20	Not used	Orthomosaic did not stitch together due to high tide and wind

I used two imagery sets for the pixel-based analysis. The first included the “full season” dataset as described in Table 4. The second includes only the transect 1 area of the July 4 imagery and will be referred to by that date. I chose to analyze the imagery in this way to allow a comparison of the predictive ability of the full season versus a single flight, and to evaluate the predictive power accordingly. I used the July 4 imagery because there more ground-truth data

available for that date, since the annual PB-NERR biomonitoring data collection took place on July 4 and 5, 2020 and they granted me use of their percent cover data.

### 3.1.2 | Optimal flight parameters

Over the course of the season, the flights began earlier in the day which resulted in lower solar angles at the beginning and end of the flight (Table 5). The overall change in solar angle during the flight increased over the season, from a change of  $+0.53^{\circ}$  on June 7 to  $+13.53^{\circ}$  on August 29 (Table 5). Notably, the sun angle remained below  $52^{\circ}$  for the entirety of both the August 1 and August 18 flights (Table 5). In contrast, the sun angle during the June flights was  $> 62^{\circ}$  and, for the July flights, changed from  $50\text{-}55^{\circ}$  at the beginning of each flight to  $61^{\circ}$  at the conclusion of these flights (Table 5). For all four of these flights, sun glint was a significant issue (Figure 12-15). Also, the minimum tide measurement for the June and July flights was below -2, whereas the minimum tides on August 1 and August 18 were -1.9 and -1.7, respectively (Table 5). The June 24 flight was conducted much later in the day specifically to try and achieve a sun angle lower than  $40^{\circ}$  as suggested by Nahirnick et al. (2019). I was unable to generate an orthomosaic from the resulting images, probably due to the deeper water (+5.0 above MLLW) which obscured much of the detail in the eelgrass beds. Similarly, I was unable to generate an orthomosaic for the August 29 flight when the tide stage was at -0.9 feet and there were significant wind-generated surface waves (Figure 4). These results suggest that a sun angle of less than  $52^{\circ}$  and a tide lower than -0.9, and perhaps closer to -1.7 as on the August 18 flight, is needed to minimize sun glint and provide sufficient detail to generate an orthomosaic.

Table 5. Imagery collection dates, tide measure, start and end time, maximum wind speed, and solar angles from the summer 2020 field season. Flights began 90 minutes prior to low tide to ensure all images would be taken before the tide began to flood. The tide measure is the level at the end of each flight. Flights on all dates except for 6/24/2020 and 8/29/2020 produced imagery that could be stitched into an orthomosaic.

<b>Date</b>	<b>Min height (ft above MLLW)</b>	<b>Start Time</b>	<b>End Time</b>	<b>Maximum wind speed (m/s)</b>	<b>Solar Angle at Start of Flight</b>	<b>Solar Angle at End of Flight</b>
6/7/20	-2.8	12:20 PM	1:50 PM	1.8	62.55	63.08
6/23/20	-2.3	12:40 PM	2:10 PM	6.0	64.08	62.43
6/24/20	+5.0	6:05 PM	7:35 PM	3.5	38.23	23.41
7/4/20	-2.7	10:40 AM	12:10 PM	1.0	50.1	61.24
7/21/20	-2.3	11:40 AM	1:10 PM	1.5	55.75	61.71
8/1/20	-1.9	9:45 AM	11:15 AM	2.0	37.58	50.62
8/18/20	-1.7	10:40 AM	12:10 PM	4.5	42.21	51.88
8/29/20	-0.9	8:55 AM	10:25 AM	6.5	23.91	37.44

Given these results, I wanted to know if it would have theoretically been possible to schedule 2020 flights that met the following criteria: 1) tide state close to -1.9 ft, with “close” defined as  $\pm 0.5$  ft, and 2) sun angle lower than  $52^\circ$ . As shown in Table 5, there were four times in 2020 that met all three criteria (April 11, July 2, July 19, and August 18), as well as three dates that met criteria 1) but had a maximum sun angle slightly higher than  $52^\circ$  (May 7, June 4, and August 3).

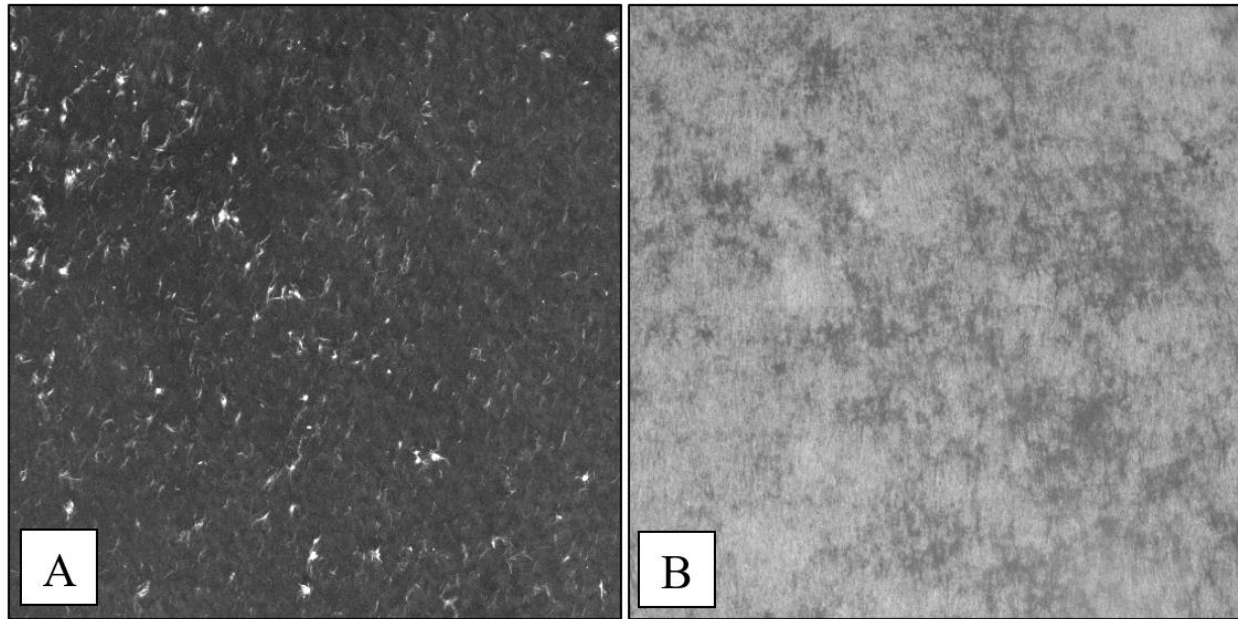


Figure 4. Near infrared images captured during data collection over the same area for the A) low sun angle flight on June 24, 2020; tide at +5.0 ft above MLLW and B) low tide flight on August 1, 2020; tide at -1.9 ft above MLLW.

Table 6. Actual and theoretical data collection dates in 2020 that 1) occur during daylight hours and 2) have a tide no lower than -1.9 ft. The April 11, July 2, July 19, and August 18 theoretical flights also have sun angles lower than  $52^\circ$ .

<b>Date</b>	<b>Min height (ft above MLLW)</b>	<b>Start Time</b>	<b>End Time</b>	<b>Solar Angle at Start of Flight</b>	<b>Solar Angle at End of Flight</b>
Best quality flights of 2020:					
8/1/2020	-1.9	9:45 AM	11:15 AM	37.58	50.62
8/18/2020	-1.7	10:40 AM	12:10 PM	42.21	51.88
Theoretical flights:					
4/11/2020	-1.4	1:05 PM	2:35 PM	50.17	46.44
5/7/2020	-1.4	10:29 AM	11:59 PM	45.19	55.68
6/4/2020	-1.9	9:29 AM	10:59 AM	39.74	53.50
7/2/2020	-1.7	8:29 AM	9:59 AM	29.23	43.95
7/19/2020	-1.8	9:32 AM	11:02 AM	37.61	51.30
8/3/2020	-1.7	10:19 AM	11:49 AM	42.95	54.02
8/18/2020	-1.7	9:50 AM	11:20 AM	34.96	47.19

### 3.2 | Epiphyte load

To quantify seasonal variation in epiphyte load over the course of the season, I standardized the dry weights of epiphytes as a percentage of the total above ground dry weight of the individual plant from which they were scraped. This allowed me to compare epiphyte load throughout the season while taking increasing plant size into account as well. Epiphyte load ranged from 0% to 80.4% for *Z. japonica* and from 0% to 68.8% for *Z. marina*. A one-way ANOVA was conducted to compare the effect of date on epiphyte load for *Z. japonica* and *Z. marina*. There was not a statistically significant difference in epiphyte load on either *Z. japonica* ( $F(2, 160) = 1.138, p = 0.32$ ) or *Z. marina* ( $F(2, 160) = 0.513, p = 0.6$ ) samples between the three biomass collection dates (Figure 5).

I also plotted epiphyte load for each species as a function of the elevation above MLLW (m) (Figure 6). Elevation data were obtained from PB-NERR and represent the elevation at the PVC post marking the plot. I ran a simple linear regression on epiphyte load and elevation above MLLW and found a significant but very weak relationship between the two variables for *Z. japonica* ( $R^2 = 0.05, p < 0.05$ ) and a significant but weak relationship between the two variables for *Z. marina* ( $R^2 = 0.33, p < 0.001$ ). However, I did observe a stronger relationship between *Z. marina* epiphyte load and elevation above MLLW for the August ground truth data ( $R^2 = 0.63, p < 0.001$ ) (Figure 7).



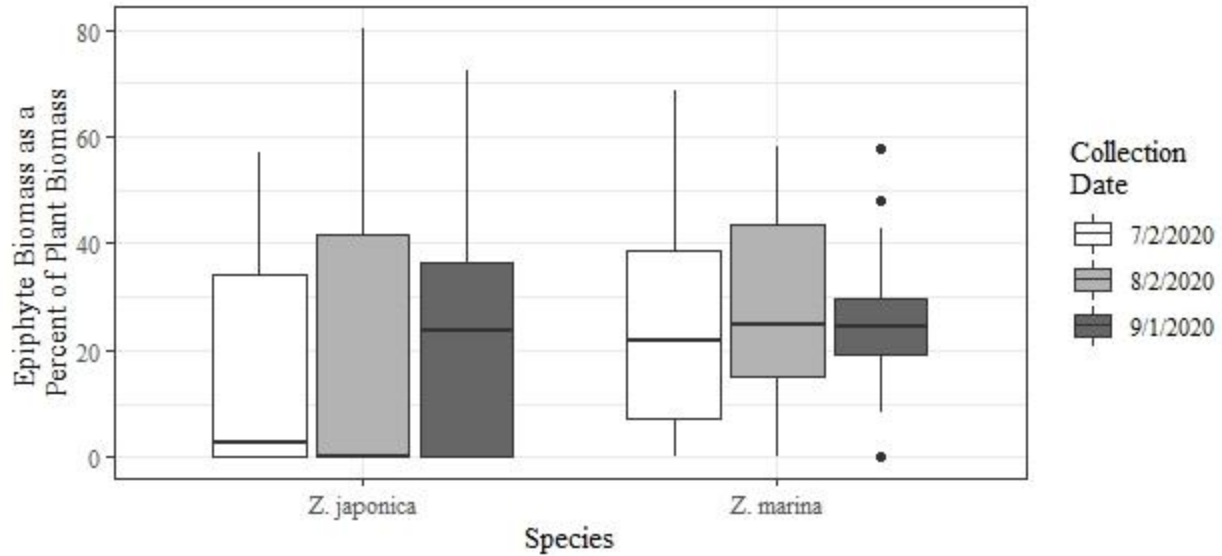


Figure 5. Epiphyte biomass as a percent of plant biomass for *Z. japonica* and *Z. marina* samples collected on July 2, August 2, and September 1, 2020. The center line of the boxplot is the median and the lower and upper bounds of the box are the lower (25<sup>th</sup> percentile) and upper (75<sup>th</sup> percentile) quartile values, respectively. The whiskers extend 1.5 times the interquartile range above the upper quartile and below the lower quartile. Outliers are represented by dots.

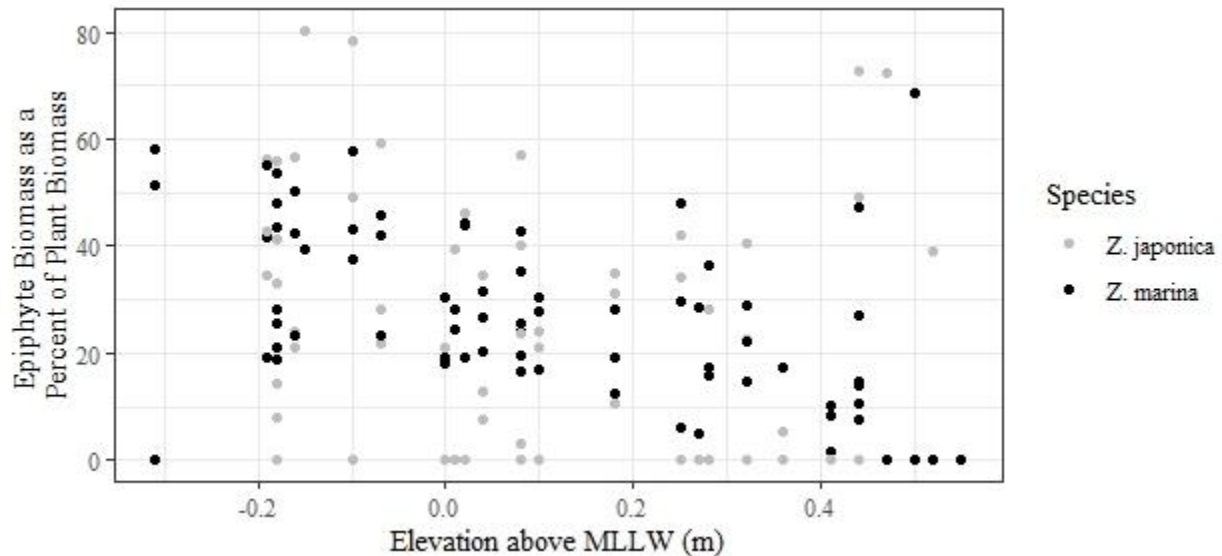


Figure 6. Epiphyte biomass as a percent of plant biomass for *Z. japonica* and *Z. marina* samples as a function of elevation above mean lower low water (m) (MLLW). A simple linear regression shows a significant but very weak between epiphyte load on *Z. japonica* and elevation above MLLW ( $R^2 = 0.05$ ,  $p < 0.05$ ) and a significant but weak relationship between epiphyte load on *Z. marina* and elevation above MLLW ( $R^2 = 0.33$ ,  $p < 0.001$ ).

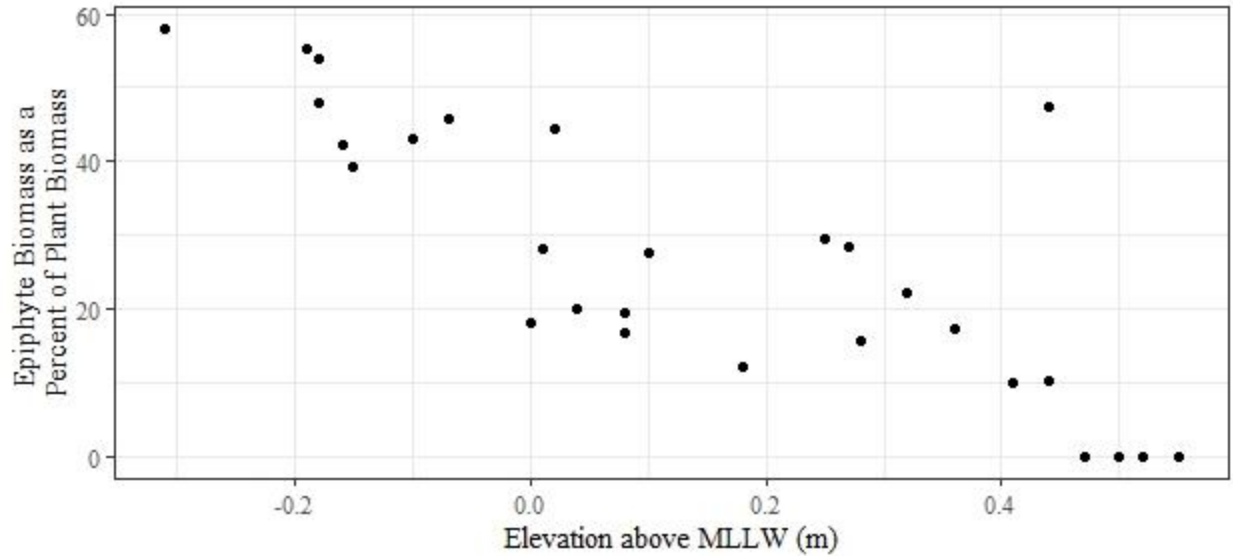


Figure 7. Epiphyte biomass as a percent of plant biomass for *Z. marina* samples collected on August 2, 2020, as a function of elevation above mean lower low water (m) (MLLW). A simple linear regression shows a moderate relationship between epiphyte load and elevation above MLLW (m) for *Z. marina* in August ( $R^2 = 0.63$ ).

### 3.3 | Principal component analysis

I conducted two PCAs in ENVI: one using the full season set of imagery and one using July 4 imagery. These PCAs will be referred to as the “full season PCA” and the “July 4 PCA”. I chose to do a separate PCA for the July 4 imagery so that I could compare the predictive strength of the full season models with the strength of a single date model. July 4 is the only date for which I had sufficient ground control data for a single date analysis. Much of the variance in the full season dataset results from variation in the sun angle and wind-driven waves. Since the PCA is based upon the total variance in the imagery, I needed to conduct separate PCAs on each imagery set to obtain accurate results. The loadings for the first three principal components of the full season PCA have distinct characteristics. The first principal component explains 60.84% of the variance (Table 7). All bands have negative loadings and are of a similar magnitude, ranging

from -0.15 to -0.39 (Table 7). The second principal component explains 35.64% of the variance (Table 7). In PC2, there are some strong contrasts between band loadings. Most notably, the red edge and NIR bands have strong negative loadings ( $< -0.34$ ) which contrast the positive loadings of the blue and red bands (Table 7). The third principal component explains only 1.61% of the variance (Table 7). In PC3 there is a strong contrast between blue, red, upper Red edge 740(18) and NIR bands with the green bands and the lower Red edge 705(10) band (Table 7).

Table 7. Loadings for the first three principal components of the PCA conducted on all 10 bands of the Micasense dual camera system for the full season mosaic of imagery (July 4, July 21, August 1, and August 18, 2020).

<b>Band</b>	<b>PC1</b>	<b>PC2</b>	<b>PC3</b>
Coastal blue 444(28)	-0.374499	0.1685	0.352719
Blue 475(32)	-0.358578	0.235164	0.191769
Green 531(14)	-0.394088	0.083382	-0.260399
Green 560(27)	-0.38776	-0.015717	-0.668404
Red 650(16)	-0.359298	0.229755	0.015903
Red 668(14)	-0.336719	0.277639	0.357799
Red edge 705(10)	-0.296861	-0.34658	-0.165945
Red edge 717(12)	-0.206621	-0.450194	-0.017857
Red edge 740(18)	-0.166163	-0.478431	0.180082
NIR 842(57)	-0.156863	-0.47702	0.368352
<b>% variance explained</b>	60.84	35.64	1.61

The results of the July 4 PCA are extremely similar to those of the full season, but the patterns for PC1 and PC2 are switched. In the July 4 PCA, PC1 accounts for 64.34% of the variance and has strong contrasts between all the bands in the visible part of the spectrum (blue, green, and red) with the red edge and NIR bands (Table 8). The second principal component explains 35.53% of the variance. All loadings are negative and range from -0.08 to -0.52 (Table 8). The third principal component explains only 0.71% of the variance but has a notable contrast

between the loadings of the Green 560(27) and Red edge 705(10) bands with the NIR 842(57) band (Table 8). Hence, the pattern of loadings on PC3 are similar for both the July 4 PCA and the full season PCA but with the signs reversed.

Table 8. Loadings for the first three principal components of the PCA conducted on all 10 bands of the Micasense dual camera system for only the July 4 imagery.

<b>Band</b>	<b>PC1</b>	<b>PC2</b>	<b>PC3</b>
Coastal blue 444(28)	0.377443	-0.139424	-0.098346
Blue 475(32)	0.382378	-0.120551	-0.140781
Green 531(14)	0.353420	-0.230517	0.107712
Green 560(27)	0.316061	-0.310027	0.214870
Red 650(16)	0.383375	-0.104697	-0.181778
Red 668(14)	0.387192	-0.076711	-0.279207
Red edge 705(10)	-0.070835	-0.525576	0.612962
Red edge 717(12)	-0.243349	-0.424798	0.051650
Red edge 740(18)	-0.254517	-0.412266	-0.302012
NIR 842(57)	-0.246200	-0.416270	-0.576313
<b>% variance explained</b>	64.34	33.53	0.71

### 3.4 | Pixel-based analysis

#### 3.4.1 | Total eelgrass cover

For both the full season of imagery and for the July 4 subset, I created 18 regression models and compared their efficacy at predicting total eelgrass cover (Table 9). These models used all 10 bands of the Micasense camera, all available permutations of NDVI and NDRE given the Micasense bands, as well as combinations of the first three PCs. Equations for the most effective models for each predictor variable category are presented in Table 10. Generally, the July 4 models outperformed the full season models for all types of predictor variables (Table 9). Individually, the raw band data for the full season did not perform well. But for the July 4 subset, using individual bands as predictor variables yielded decent results, with all but one model

having an  $R^2$  greater than 0.6 (Table 9). I explored multiple band combinations and found that using the Red 650(16) and Red edge 717(12) bands together had the highest  $R^2$ , with  $R^2 = 0.79$  and  $R^2 = 0.89$ , for the full season and July 4 images, respectively (Table 9). This combination also yielded variance inflation factors (VIF) less than 4, which indicates the absence of collinearity in the predictors. All combinations of three or more bands were collinear and were not considered in this analysis.

The PCA results for the July 4 subset yielded the next best results, with the model utilizing PC1 and PC3 yielding an  $R^2$  of 0.887 (Table 9). The full season model using PC1 and PC2 had an  $R^2$  of 0.71 (Table 9). Overall, using the first three principal components as predictor variables yielded an  $R^2$  of 0.75 for the full season and 0.885 for July 4 (Table 9). It is noteworthy that although PC3 captured a very small percentage of the variance for both the full season (Table 7) and July 4 (Table 8) PCAs it was included in the best PCA models and the magnitude of the coefficient for PC3 in these models is comparable to the loadings for the other PCs that captured a much higher percentage of the variance (Table 10). For the full season model, the magnitude of the coefficient for PC3 is roughly three times greater than the coefficient for PC1 even though PC1 captures 60% of the variance in the imagery vs. only 1.6% of the variance for PC3. For the July 4 model, the coefficient for PC1, which captures 64% of the variance in the imagery is roughly 50% greater than the magnitude of the coefficient for PC3, which captures only 0.7% of the variance in the imagery. This suggests that, although PC3 captures very little variance in the imagery, it is capturing an important bit of information.

Using NDVI also proved to be an effective method to predict total eelgrass cover. The effectiveness of using NDVI to predict total eelgrass cover did not seem to depend on which red band was used in the calculation. For the full season, using NDVI as the predictor variable had

an  $R^2$  of 0.763 when calculated with the Red 650(16) band and an  $R^2$  of 0.759 when calculated with the Red 668(14) band (Table 8). For the July 4 subset, the NDVI calculated with the Red 650(16) band resulted in an  $R^2$  of 0.872 and the NDVI using the Red 668(14) had an  $R^2$  of 0.875 (Table 8).

Unlike the NDVI models, the efficacy of the NDRE models changed drastically with the choice of red edge band used in the calculations. The NDRE models using the Red edge 705(10) band performed decently, with an  $R^2$  of 0.62 and 0.76 for the full season and July 4 datasets, respectively (Table 9). Using the Red edge 717(12) band resulted in a weak relationship between NDRE and total eelgrass cover, with an  $R^2$  of 0.36 and 0.47 for the full season and July 4 datasets, respectively (Table 9). Models using the NDRE calculated with the Red edge 740(18) band had no relationship with total eelgrass cover, with an  $R^2$  of 0.06 and -0.02 for the full season and July 4 datasets, respectively (Table 9).

#### 3.4.2 | *Z. japonica* cover

Pixel-based regression models performed very poorly at predicting *Z. japonica* percent cover. All modeling efforts resulted in  $R^2$  below 0.33, with most around 0.1 (Table 11). Overall, the highest  $R^2$  were seen in models using the blue bands (Table 11). There does not appear to be a difference in overall efficacy between the full season and July 4 models.

#### 3.4.3 | *Z. marina* cover

Overall, using the July 4 subset resulted in more effective *Z. marina* percent cover predictive models than the full season of imagery. However, the best models had mediocre  $R^2$  values. The model using PC2 and PC3 had the highest  $R^2$  of all full season models with 0.48 (Table 12). For the July 4 subset, the best model used the NDVI calculated with the Red 650(16) band and had an  $R^2$  of 0.56 (Table 12).

Table 9. Summary of regression models used to predict total eelgrass cover for the full season mosaic of imagery and for the July 4 subset. The number after the band name is the central wavelength, and the number in parentheses is the band width. For the full season, n=101, and for July 4, n=40. Highlighted rows indicate the best model for each category of predictor variable for the full season and for the July 4 data.

Predictor variable(s)	Full season			July 4		
	Adjusted R <sup>2</sup>	F-statistic	p-value	Adjusted R <sup>2</sup>	F-statistic	p-value
Coastal blue 444(28)	0.14	16.94	< 0.001	0.83	194	< 0.001
Blue 475(32)	0.24	33.67	< 0.001	0.85	219.5	< 0.001
Green 531(14)	0.05	6.395	0.013	0.77	130	< 0.001
Green 560(27)	-0.005	0.49	0.48	0.65	74.7	< 0.001
Red 650(16)	0.29	42.68	< 0.001	0.87	258.5	< 0.001
Red 668(14)	0.36	58.96	< 0.001	0.88	283	< 0.001
Red edge 705(10)	0.24	33.67	< 0.001	0.33	20.33	< 0.001
Red edge 717(12)	0.48	95.35	< 0.001	0.67	81.48	< 0.001
Red edge 740(18)	0.52	111.2	< 0.001	0.66	78.28	< 0.001
NIR 842(57)	0.49	98.89	< 0.001	0.61	63.04	< 0.001
Red 650(16) + Red edge 717(12)	0.79	195.1	< 0.001	0.89	164.6	< 0.001
NDVI <sub>5,10</sub>	0.763	326.2	< 0.001	0.872	265.6	< 0.001
NDVI <sub>6,10</sub>	0.759	319.2	< 0.001	0.875	273.4	< 0.001
NDRE <sub>7,10</sub>	0.62	165	< 0.001	0.76	125.7	< 0.001
NDRE <sub>8,10</sub>	0.36	57.05	< 0.001	0.47	36.19	< 0.001
NDRE <sub>9,10</sub>	0.06	7.39	0.008	-0.02	0.33	0.57
PC1	0.01	2.325	0.1304	0.86	249.7	< 0.001
PC2	0.61	158.5	< 0.001	0.45	32.38	< 0.001
PC3	0.40	69.26	< 0.001	0.51	41.67	< 0.001
PC1 + PC2	0.71	125.2	< 0.001	0.882	147.3	< 0.001
PC1 + PC3	0.45	42.42	< 0.001	0.887	154.6	< 0.001
PC2 + PC3	0.66	99.28	< 0.001	0.53	23	< 0.001
PC1 + PC2 + PC3	0.75	100.6	< 0.001	0.885	101.1	< 0.001

Table 10. Equations for the most effective regression model for band data, NDVI, NDRE, and PCA used to predict total eelgrass cover. The number after the band name is the central wavelength, and the number in parentheses is the band width. The subscript numbers after the vegetation indices refer to the band numbers used to calculate the index.

Predictor variable(s)	Equation	Adjusted R <sup>2</sup>
Full season		
Red 650(16) + Red edge 717(12)	Total % cover = $46.7 - 1804.6 * \text{"Red 650(16)"} + 1048.9 * \text{"Red edge 717(12)"} + 1048.9$	0.79
NDVI <sub>5,10</sub>	Total % cover = $15.6 + 135.5 * NDVI_{5,10}$	0.76
NDRE <sub>7,10</sub>	Total % cover = $36.2 + 251.6 * NDRE_{7,10}$	0.62
PC1 + PC2 + PC3	Total % cover = $74.6 + 405.9 * PC1 - 1087.7 * PC2 - 1562.4 * PC3$	0.75
July 4		
Red 650(16) + Red edge 717(12)	Total % cover = $98.7 - 2943.6 * \text{"Red 650(16)"} + 655.3 * \text{"Red edge 717(12)"} + 655.3$	0.89
NDVI <sub>6,10</sub>	Total % cover = $-11.9 + 143.9 * NDVI_{6,10}$	0.87
NDRE <sub>7,10</sub>	Total % cover = $11.2 + 313.1 * NDRE_{7,10}$	0.76
PC1 + PC3	Total % cover = $62.4 - 1557.5 * PC1 + 942.8 * PC3$	0.887



Table 11. Summary of regression models used to predict *Z. japonica* cover for the full season mosaic of imagery and for the July 4 subset. The number after the band name is the central wavelength, and the number in parentheses is the band width. For the full season, n=101, and for July 4, n=40. Highlighted rows indicate the best model for each category of predictor variable for the full season and for the July 4 data.

Predictor variable(s)	Full season			July 4		
	Adjusted R <sup>2</sup>	F-statistic	p-value	Adjusted R <sup>2</sup>	F-statistic	p-value
Coastal blue 444(28)	0.019	2.95	0.09	0.21	11.44	0.002
Blue 475(32)	0.32	4.37	0.04	0.2	10.65	0.002
Green 531(14)	0.012	2.27	0.14	0.14	7.10	0.01
Green 560(27)	0.0042	1.43	0.23	0.08	4.58	0.04
Red 650(16)	0.053	6.62	0.01	0.18	9.74	0.003
Red 668(14)	0.04	5.17	0.03	0.19	10.07	0.003
Red edge 705(10)	-0.01	0.012	0.91	0.0097	1.38	0.25
Red edge 717(12)	0.0028	1.29	0.26	0.1	5.46	0.03
Red edge 740(18)	0.016	2.69	0.10	0.12	6.11	0.02
NIR 842(57)	0.018	2.86	0.09	0.099	5.27	0.03
NDVI <sub>5,10</sub>	0.054	6.74	0.01	0.1	7.77	0.008
NDVI <sub>6,10</sub>	0.044	5.69	0.02	0.15	8.06	0.007
NDRE <sub>7,10</sub>	0.066	8.13	0.005	0.13	6.88	0.01
NDRE <sub>8,10</sub>	0.23	3.38	0.07	0.051	3.083	0.09
NDRE <sub>9,10</sub>	-0.001	0.0027	0.96	-0.019	0.29	0.59
PC1	-0.0061	0.39	0.54	0.17	8.76	0.005
PC2	0.02	3.07	0.08	0.058	3.40	0.07
PC3	0.026	3.74	0.06	0.081	4.43	0.04
PC1 + PC2	0.045	3.36	0.04	0.16	4.65	0.02
PC1 + PC3	0.055	3.95	0.02	0.15	4.54	0.02
PC2 + PC3	0.017	1.86	0.16	0.086	2.83	0.07
PC1 + PC2 + PC3	0.046	2.61	0.06	0.14	3.04	0.04

Table 12. Summary of regression models used to predict *Z. marina* cover for the full season mosaic of imagery and for the July 4 subset. The number after the band name is the central wavelength, and the number in parentheses is the band width. For the full season, n=101, and for July 4, n=40. Highlighted rows indicate the best model for each category of predictor variable for the full season and for the July 4 data.

Predictor variable(s)	Full season			July 4		
	Adjusted R <sup>2</sup>	F-statistic	p-value	Adjusted R <sup>2</sup>	F-statistic	p-value
Coastal blue 444(28)	0.05	6.34	0.013	0.46	33.79	< 0.001
Blue 475(32)	0.10	12.73	< 0.001	0.48	37.37	< 0.001
Green 531(14)	0.0063	1.64	0.2	0.48	37	< 0.001
Green 560(27)	-0.0095	0.046	0.83	0.44	31.87	< 0.001
Red 650(16)	0.11	13.63	< 0.001	0.51	42.32	< 0.001
Red 668(14)	0.17	22.43	< 0.001	0.52	42.8	< 0.001
Red edge 705(10)	0.24	33.24	< 0.001	0.25	14.24	< 0.001
Red edge 717(12)	0.35	55.75	< 0.001	0.44	31.11	< 0.001
Red edge 740(18)	0.34	52.72	< 0.001	0.41	28.37	< 0.001
NIR 842(57)	0.31	46.6	< 0.001	0.39	25.73	< 0.001
NDVI <sub>5,10</sub>	0.44	79.62	< 0.001	0.56	49.79	< 0.001
NDVI <sub>6,10</sub>	0.45	85.11	< 0.001	0.55	49.16	< 0.001
NDRE <sub>7,10</sub>	0.31	46.76	< 0.001	0.48	36.94	< 0.001
NDRE <sub>8,10</sub>	0.2	25.78	< 0.001	0.32	19.69	< 0.001
NDRE <sub>9,10</sub>	0.05	6.83	0.01	-0.0008	0.97	0.33
PC1	0.03	3.93	0.05	0.53	44.83	< 0.001
PC2	0.4	67.77	< 0.001	0.29	16.82	< 0.001
PC3	0.22	30.29	< 0.001	0.32	19.2	< 0.001
PC1 + PC2	0.42	38.07	< 0.001	0.52	22.42	< 0.001
PC1 + PC3	0.22	15.49	< 0.001	0.53	22.9	< 0.001
PC2 + PC3	0.48	47	< 0.001	0.31	9.65	< 0.001
PC1 + PC2 + PC3	0.49	33.62	< 0.001	0.52	15.2	< 0.001

### 3.5 | Object-based image analysis

I segmented the full season imagery in four different ways, each using a different predictor variable source to inform the multiresolution segmentation process. To mirror the pixel-based analysis, I did a segmentation based on band data, NDVI, NDRE, and PCA. For the NDVI-based segmentation, I used NDVI<sub>6,10</sub> because it visually did a better job of defining vegetated areas. For the NDRE-based segmentation, I used NDRE<sub>7,10</sub> because, as shown in the pixel-based analysis results, it outperformed the other two NDRE versions (Table 9).

Ground truth data were subset to the 85 plots with at least 80% of total vegetative cover since the purpose of this analysis is to determine whether it is possible to define areas of *Z. marina* and *Z. japonica* separately from each other. I masked the bare area in the imagery prior to performing the segmentation process using an NDVI threshold of 0.15, and so theoretically, the segments I classified during this analysis were fully vegetated, or nearly so. However, some ground plots contained algae and detritus and it is reasonable to assume that the masking process of the bare area was not perfect, and some bare areas might be present in the image segments. For these reasons, I decided to set the threshold of vegetation at 80% to allow for the inclusion of other cover types in small percentages.

There were 16 ground truth plots that contained less than 80% of vegetated cover that were not used in training or testing the SVM. Six of these plots were completely bare and were located within the area delineated as “bare” through the NDVI masking in eCognition. Since the SVM was developed only to classify within vegetated areas, the bare ground truth plots were not used. The other 10 plots were sparsely vegetated and were found in areas that contained small segments at the threshold between bare and vegetated areas in Padilla Bay. Since these plot

polygons were each intersected by multiple image segments, they were not used as ground truth since they were associated with more than one segment.

### 3.5.1 | Accuracy of object-based image analysis methods

After ground truth data were subset according to their level of overall vegetation, I tested several methods of categorizing the plots based on whether they were *Z. japonica* dominant, *Z. marina* dominant, or mixed. The definitions used to place ground truth plots in these categories are presented in Table 13. Overall, using method 3 of ground truth categorization produced the most accurate classifications (Table 14). User's, producer's, and overall accuracies for the NDRE, NDVI, and PCA segmentations based on categorization method 3 are presented in Table 15. Confusion matrices for results for all categorization methods are available in the appendix.

Table 13. Criteria used to categorize the vegetation type in ground truth plots that were at least 80% vegetated. The categorization will be used to inform segmentation classification.

Method #	<i>Z. japonica</i> dominant	<i>Z. marina</i> dominant	Mixed
			Split into two categories:
1	>80% of total cover	>80% of total cover	<div> <div> <u><i>Z. japonica</i> dominated</u>  50-80% of total cover  is <i>Z. japonica</i> </div> <div> <u><i>Z. marina</i> dominated</u>  50-80% of total cover  is <i>Z. marina</i> </div> </div>
2	>80% of total cover	>80% of total cover	Either <i>Z. japonica</i> or <i>Z. marina</i> has 50-80% of the total cover
3	>90% of total cover	>90% of total cover	Neither <i>Z. japonica</i> nor <i>Z. marina</i> has >90% of the total cover
4	>70% of total cover	>70% of total cover	Neither <i>Z. japonica</i> nor <i>Z. marina</i> has >70% of the total cover

Table 14. Summary of overall percent classification accuracy for the four ground truth categorization methods and the four image segmentation types for classification informed by mean value for all pixels in a segment.

Method #	Segmentation method			
	Band	NDVI <sub>6,10</sub>	NDRE <sub>7,10</sub>	PCA
1	57.8	51.3	55.6	58.8
2	60.2	57.7	63.0	68.2
3	60.2	64.1	70.3	70.6
4	57.8	58.2	69.1	68.6

The SVM classification based on the band segmentation and the mean band values for each segment was somewhat accurate overall, with a total accuracy of 60.2% (Table 15). While the producer's accuracy for *Z. japonica* dominant plots was high, the user's accuracy for this category was low (57.1%) and was commonly misclassified as *Z. marina* dominant (Table 15). Classification between *Z. marina* dominant and mixed plots was muddled, with producer's and user's accuracies for these categories between 54.5 and 64.9% (Table 15). Using the 10 band means and the 10 band standard deviations drastically improved the accuracy of the classification to 78.3% overall (Table 15). This method also improved or maintained the user's and producer's accuracies for all classes (Table 15).

The SVM classification based on the NDVI<sub>6,10</sub> segmentation was 64.1% accurate overall for both the classification using only the mean NDVI<sub>6,10</sub> for each segment and the classification using the mean and standard deviation of NDVI<sub>6,10</sub> for each segment as predictor variables (Table 15). While the overall result is decent, the classification accuracy for identifying *Z. japonica* is very poor, with a user's accuracy of 25.0% for both sets of predictors (Table 15). Using the mean NDVI<sub>6,10</sub> resulted in a low producer's accuracy for mixed plots as well, at only

48.6%, but had a very high user's accuracy for that category at 80.9% (Table 15). The user's and producer's accuracies for classifying *Z. marina* and mixed plots using mean and standard deviation are between 59.5 and 74.3%, which is slightly worse than the results from the NDRE based segmentation (Table 15).

Classifying segments based on the NDRE<sub>7,10</sub> was accurate overall with a total accuracy of 70.3% using the mean NDRE<sub>7,10</sub> for each segment and 69.1% using the mean and standard deviation of NDRE<sub>7,10</sub> for each segment (Table 15). However, when looking at the user's and producer's accuracies for the different categories, it's clear this classification does not work for identifying areas dominated by *Z. japonica*, with 0 of 8 *Z. japonica* plots identified correctly (Table 15). The *Z. marina* and mixed categories are more accurately identified using the NDRE segmentation than the band segmentation, with user's and producer's accuracies ranging from 63.0-78.4% (Table 15).

The SVM classifications based on the PCA segmentation was the second most accurate of all segmentations evaluated, at 70.6% (Table 15). While this overall result is close to the overall accuracy for the NDRE<sub>7,10</sub> segmentation (69.1%), it does a better job of identifying *Z. japonica* plots. The user's and producer's accuracies for classifying *Z. japonica* when using the means of the PCs for each segment as a predictor variable are 83.3% and 62.5%, respectively (Table 15). The user's and producer's accuracies for classifying *Z. japonica* when using the means and standard deviations of the PCs for each segment as predictor variables are both 75.0% (Table 15). Using both the means and standard deviations also appears to be the best because the user's and producer's accuracies are the most consistent for each of the three categories evaluated (Table 15).

Table 15. Summary of user's, producer's, and overall accuracy results for the SVM classifications run on all four segmentation types using ground truth categorization method 3. N = 85 for ground truth plots used to build the SVM classifier for each segmentation type.

Segmentation type	Predictor variable(s)	Cover category	Accuracy (%)		
			User's	Producer's	Overall
Band	Mean	<i>Z. japonica</i>	100.0	57.1	60.2
		<i>Z. marina</i>	54.5	64.9	
		Mixed	62.9	56.4	
	Mean & standard deviation	<i>Z. japonica</i>	100	71.4	78.3
		<i>Z. marina</i>	80.0	75.7	
		Mixed	74.4	82.1	
NDVI <sub>6,10</sub>	Mean	<i>Z. japonica</i>	100.0	25.0	64.1
		<i>Z. marina</i>	56.4	88.6	
		Mixed	80.9	48.6	
	Mean & standard deviation	<i>Z. japonica</i>	100.0	25.0	64.1
		<i>Z. marina</i>	59.5	62.9	
		Mixed	66.7	74.3	
NDRE <sub>7,10</sub>	Mean	<i>Z. japonica</i>	NA	0	70.3
		<i>Z. marina</i>	62.7	86.5	
		Mixed	83.3	69.4	
	Mean & standard deviation	<i>Z. japonica</i>	0	0	69.1
		<i>Z. marina</i>	63.0	78.4	
		Mixed	77.1	75.0	
PCA	Mean	<i>Z. japonica</i>	83.3	62.5	70.6
		<i>Z. marina</i>	65.9	78.4	
		Mixed	74.3	65.0	
	Mean & standard deviation	<i>Z. japonica</i>	75.0	75.0	70.6
		<i>Z. marina</i>	67.5	73.0	
		Mixed	73.0	67.5	

### 3.5.2 | Mapping object-based image analysis results

I applied the results of the SVM for the band and PCA informed segmentations to the entire image set and mapped them according to the predicted cover type. As previously explained, for each segmentation, I predicted cover in two ways: 1) using the mean values for the segments, and 2) using the mean values and the standard deviations for the segments. Overall, the predicted area for each cover type remained similar between the band and PCA methods (Figure 8). When using only the mean to predict cover type, the total area for each cover type for the band and PCA methods were almost identical, with *Z. marina* as the most abundant cover (93.9 and 91.2 ha, respectively) *Z. japonica* as the least (6.4 and 9.4 ha, respectively) (Figure 8, Table 16). When using the mean and standard deviation to predict cover type, the total area of the *Z. marina* and mixed categories are more similar to each other. For the band segmentation, *Z. marina* was estimated at 70.6 ha and mixed at 80.9 ha (Table 16). For the PCA segmentation, *Z. marina* was estimated at 74.7 ha and mixed at 73.4 ha (Table 16).

For all four maps, the NDVI mask applied in eCognition to delineate between bare and vegetated area is consistent, as evidenced by the identical segmentation at the transition from bare to vegetated regions (Figure 9-12). The band segmentation with the mean and standard deviation as predictor variables performed the best overall in the accuracy assessment (78.3%) with robust user's and producer's accuracies (Table 15). The map produced with this method follows the general pattern of cover type based on the PB-NERR zones, where dominant cover changes from bare, to *Z. japonica*, to mixed, to *Z. marina* moving down the intertidal (Table 1, Figure 9). With the exception of July 4, the classifier did an accurate job of identifying *Z. japonica* as the dominant cover type at the threshold between vegetated and unvegetated regions in the eastern end of the transect (Figure 9). The approach using only the band means to predict



cover type did not perform as well in the accuracy assessment overall (60.2%) or for the user's and producer's accuracies, which ranged from 54.5% – 64.9% (apart from the *Z. japonica* user's accuracy at 100%) (Table 15). These inaccuracies are visible in the map as well. For example, for July 4, almost the entire transect is predicted to be mixed and there are very small regions of *Z. marina* and *Z. japonica* (Figure 10). Furthermore, there is a very large swath of predicted *Z. marina* at the eastern end of the vegetated section of the August 18 imagery, which should be either *Z. japonica* or mixed, given its general position in the transect (Figure 10, Table 1).

While overall accuracy was the same for the PCA based segmentation and SVM classification based on mean values vs. means and standard deviations (Table 15), mapping the predicted cover shows differences between the two approaches. In the map created from predictions based on the mean values of the first three PCs, August 1 and August 18 look like what we'd expect based on the PB-NERR zones (Table 1). However, the overall pattern is different for the July 4 and July 21 imagery classifications in the vegetated area. In the July 4 classification, most of the vegetation was classified as mixed, with some clumps of *Z. marina* dominated areas in the western end and also the eastern end of the study area (Figure 11). In the July 21 classification, the majority of the vegetation was classified as *Z. marina*, with a section of *Z. japonica* at the eastern end of the vegetated area (Figure 11). Also in the July 21 classification are several *Z. japonica* dominant segments in the far western end of the transect (Figure 11). I believe these segments accurately predict the presence of *Z. japonica* in this region, since there is a higher elevation area in zone 5 where the water is shallow enough for *Z. japonica* to grow (Figure 13).

The overall patterns in the map created with the PCA segmentation and mean and standard deviation informed SVM classifier are more straightforward. For each of the imagery

dates, the cover type transitions according to the PB-NERR zones (Table 1). The main error in this version is the presence of a large swath of *Z. marina* in the southeastern corner of the vegetated area in the August 1 imagery (Figure 12).

Table 16. Predicted area and producer's accuracies for the four cover categories predicted by the SVM informed by the band and PCA segmentations. There are no producer's accuracies for the bare category because this cover type was estimated using the NDVI mask in eCognition, not with the SVM and ground truth plots.

Segmentation method	Predictor variable(s)	Cover category	Producer's accuracy (%)	Area (ha)	Area (%)
Band	Mean	Bare	N/A	36.2	18.5
		<i>Z. japonica</i>	57.1	6.4	3.3
		Mixed	56.4	59.2	30.2
		<i>Z. marina</i>	64.9	93.9	48.0
	Mean & standard deviation	Bare	N/A	36.2	18.5
		<i>Z. japonica</i>	71.4	8.0	4.1
		Mixed	82.1	80.9	41.3
		<i>Z. marina</i>	75.7	70.6	36.1
PCA	Mean	Bare	N/A	36.2	18.5
		<i>Z. japonica</i>	62.5	9.4	4.8
		Mixed	65.0	58.8	30.0
		<i>Z. marina</i>	78.4	91.2	46.6
	Mean & standard deviation	Bare	N/A	36.2	18.5
		<i>Z. japonica</i>	75.0	11.3	5.8
		Mixed	67.5	73.4	37.5
		<i>Z. marina</i>	73.0	74.7	38.2

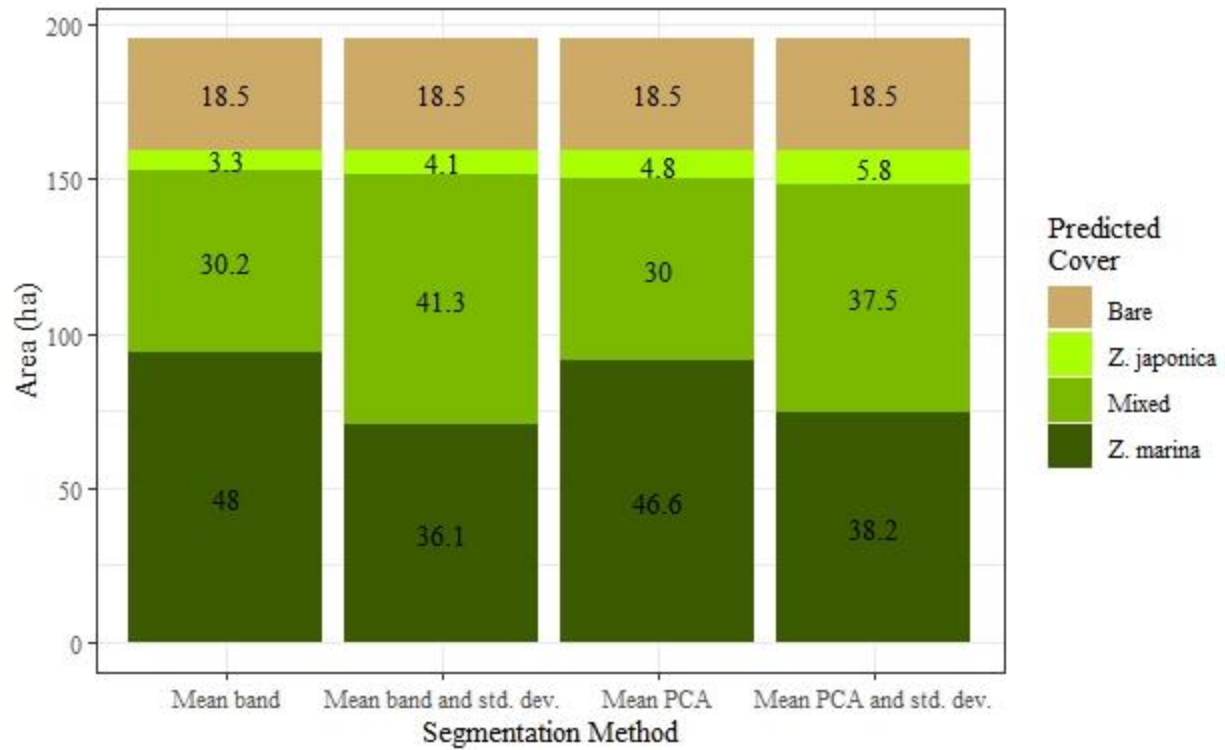


Figure 8. Predicted area for each predicted cover type for the band and PCA informed segmentation methods. Numbers presented on the bar plot represent the percent of the total area for that predicted cover type.

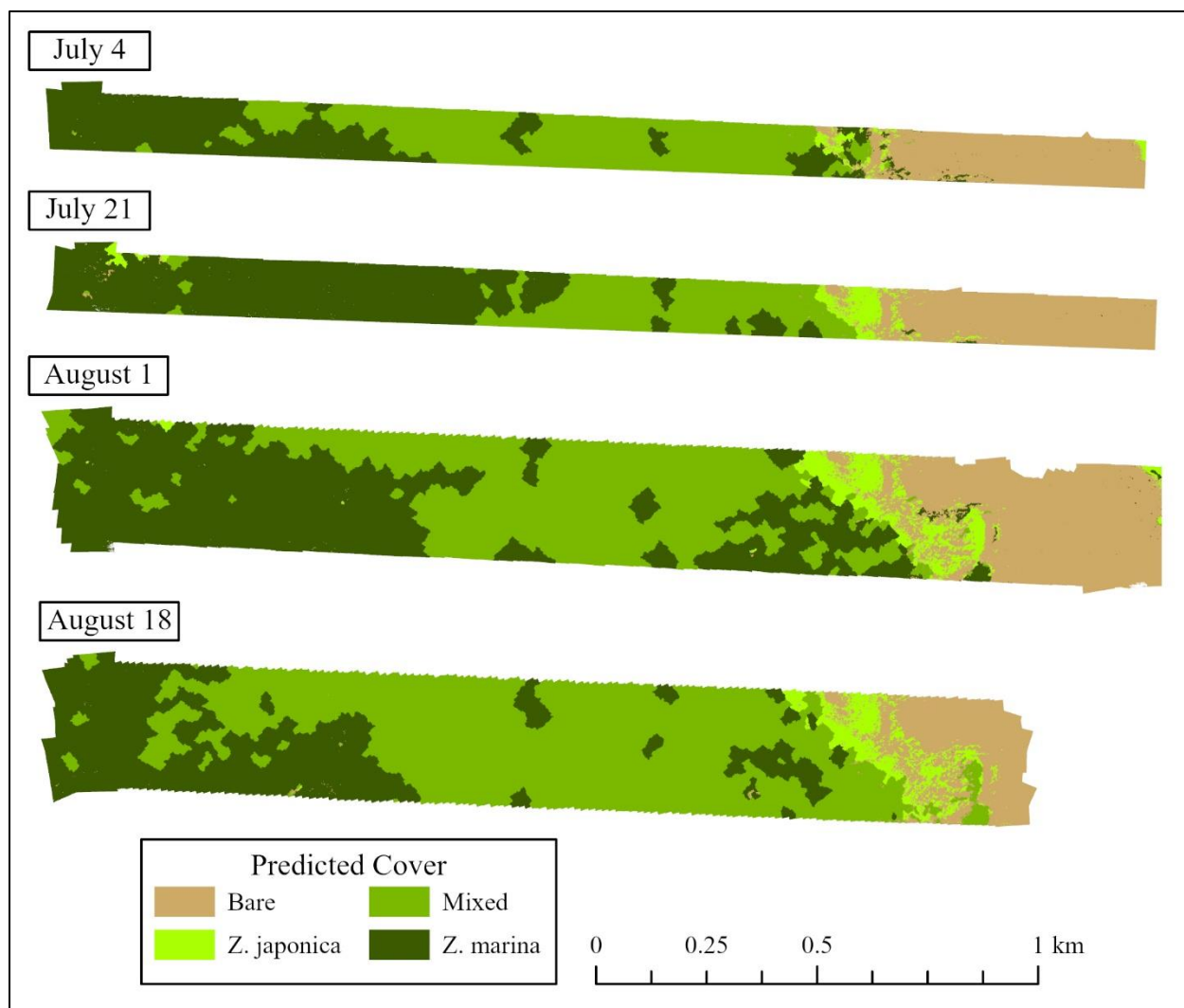


Figure 9. Map of predicted cover type classified using SVM based on raw band informed segmentation. Mean values of all 10 bands and segment standard deviations were used to train the SVM. Overall accuracy for predicting vegetation type cover for this method is 78.3%.

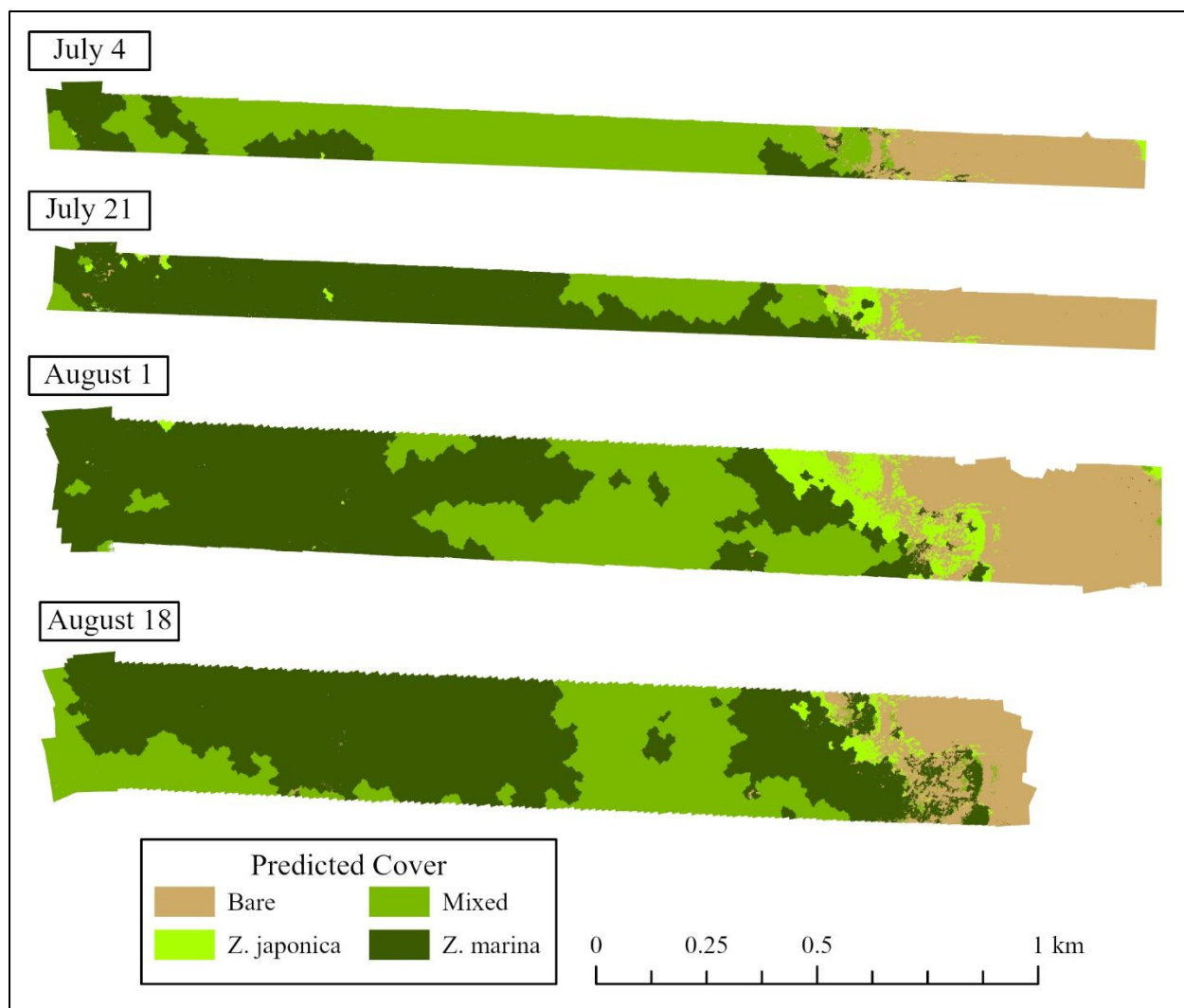


Figure 10. Map of predicted cover type classified using SVM based on raw band informed segmentation. Mean values of all 10 bands were used to train the SVM. Overall accuracy for predicting vegetation type cover for this method is 60.2%.

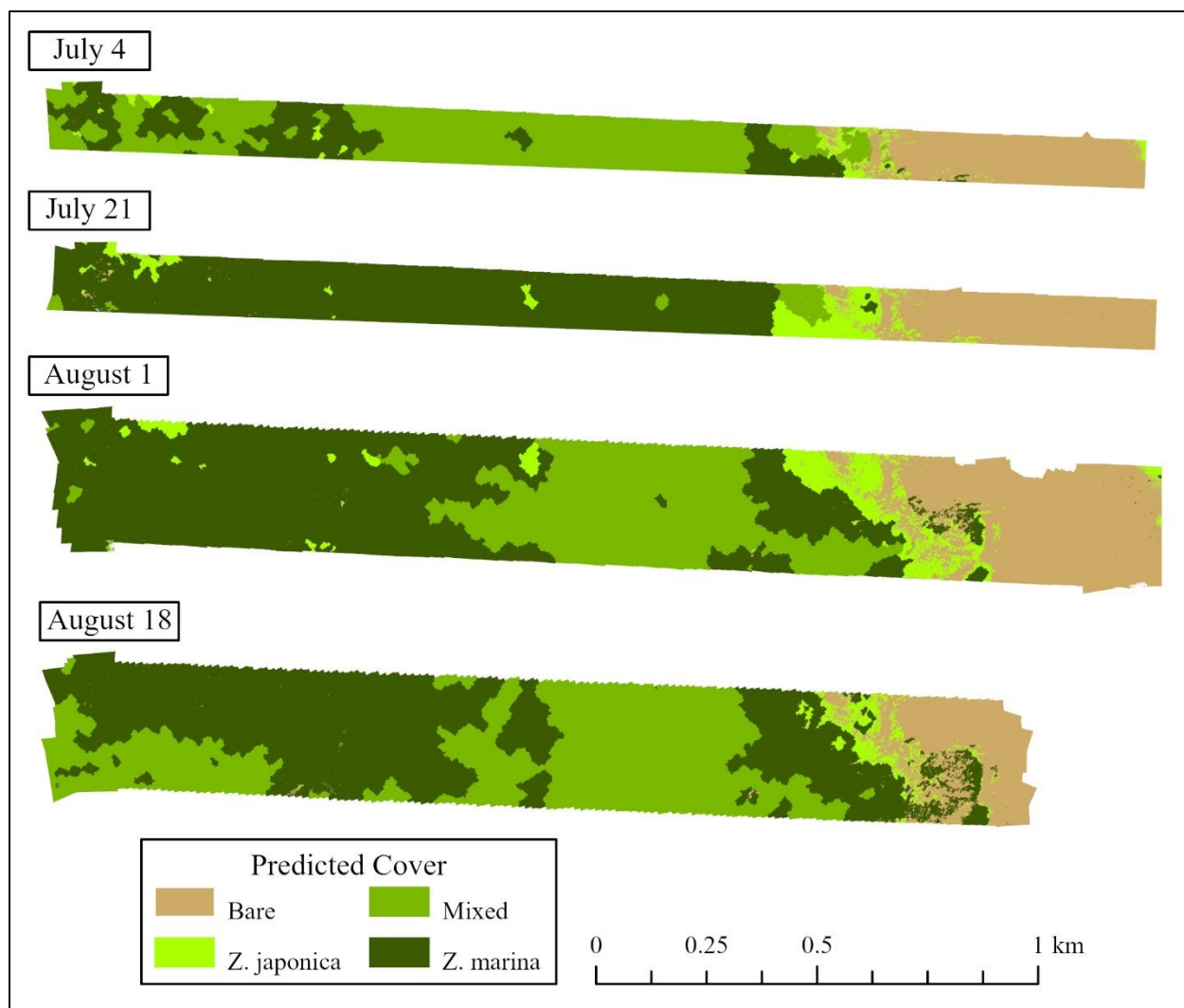


Figure 11. Map of predicted cover type classified using SVM based on PCA informed segmentation. Mean values of the first three principal components were used to train the SVM. Overall accuracy for predicting vegetation type cover for this method is 70.6%.

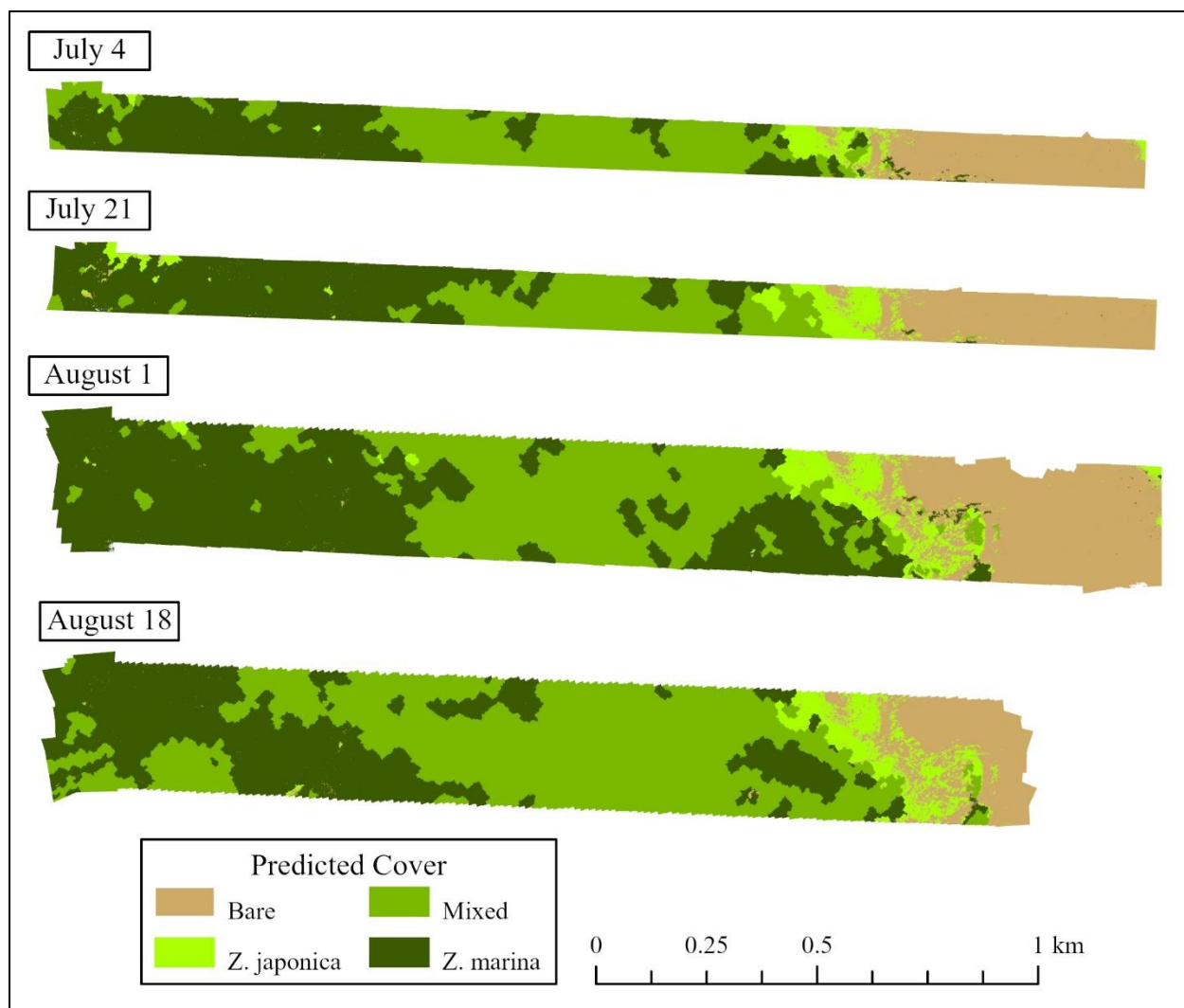


Figure 12. Map of predicted cover type classified using SVM based on PCA informed segmentation. Mean values for the first three principal components and segment standard deviations were used to train the SVM. Overall accuracy for predicting vegetation type cover for this method is 70.6%.





Figure 13. *Z. japonica* dominated area in zone 5, near plot 3.5.B. This area higher in elevation than its surroundings, allowing *Z. japonica* to grow even though it is far from shore.



## 4.0 | Discussion

The primary goals of this study were to: 1) develop models to predict percent cover of eelgrass using high-resolution multispectral imagery and 2) use these models to map the distribution and abundance of *Z. japonica* and *Z. marina* in Padilla Bay. In order to achieve these goals, I have evaluated the challenges to obtaining high-resolution multispectral imagery from a UAV in nearshore marine environments. These challenges include water depth, wind-driven waves, sun glint and variation in epiphyte load.

### 4.1 | Image collection and quality

Wind-driven waves, higher tides, and sun glint were the main challenges I faced in generating orthomosaics from the UAS imagery. In a similar study, Nahirnick et al. (2019) suggested that sun glint can be avoided by flying when sun angles are  $<40^\circ$ . However, particularly during the early summer, these sun angles only occur at higher tide stages. Following the Nahirnick et al. (2019) suggestion, my June 24 flight, which was timed to take place when the sun angle was  $<40^\circ$ , occurred at a minimum tide stage of +5 ft above MLLW. The creation of an orthomosaic requires stable tie points to match equivalent locations across the thousands of photos acquired during a flight. For this June 24 flight, deep water and waves created by wind and the flood tide created a dynamic water surface that made it impossible to locate the stable tie points needed to stitch images together into an orthomosaic (Figure 4). The Nahirnick et al. (2019) study sites were deeper than Padilla Bay and their main objective was simply to detect the presence of eelgrass and to delineate the edges of the eelgrass meadows. For their study, they chose to prioritize low sun angle and minimal wind speed to obtain imagery suitable for their study. My objective was not simply to detect eelgrass but to quantify percent cover and distinguish between *Z. japonica* and *Z. marina*. For this reason, I felt that more detailed imagery

would be needed, and I elected to fly during the lowest possible tides for each date. This resulted in sun angles that were generally greater than  $40^\circ$  and sun glint was an issue. For the June 7 and 23 flights, the very low tides enabled me to generate orthomosaics, but the sun angle was consistently  $>60^\circ$  and resulted in sun glint that made these orthomosaics unusable (Table 5). For the July flights, only the first half of the flight, when sun angles were close to  $50^\circ$ , were useable and the second half of these flights, when the sun angle was closer to  $60^\circ$  were not useable due to sun glint (Table 5).

A combination of wind-driven waves and higher tides made it impossible to generate an orthomosaic for the bare portion of the August 18 and the full August 29 imagery. Seagrass beds in shallow areas are known to attenuate waves and reduce water velocity by 60% as compared to unvegetated areas (Hansen and Reidenbach 2013). Although there was only a small amount of water on these mudflats, this difference in wave attenuation between vegetated and unvegetated areas could explain why the mudflats in the study area were more impacted visually by high wind than the eelgrass beds. For all flights with minus tides prior to August 18, lower tides (Table 5) resulted in completely dewatering the mudflats and I was successful in mosaicking the imagery for the area covered by mudflats as well as the rest of the study area (Figure 14-18).

The sun glint filter I applied to the successful orthomosaics worked well at eliminating the most affected pixels. Unfortunately, eliminating areas of sun glint decreased the number of ground truth plots that were usable for the July flights. I looked specifically at ground truth plots that lost pixels due to the sun glint filtering and found that the remaining pixels were, on average, much higher in reflectance than the ground truth plots that did not lose pixels to filtering. This suggests that even after the glint filtering process, there was still an impact of the sun glint on the remaining pixels. Thus, I decided not to use these plots for model development since the spectral

data from these plots was still impacted by sun glint. This left me with 21 of my own July ground truth plots, along with 30 ground truth plots monitored by PB-NERR in the study area. The August 1 and August 18 flights seemed to be least impacted by sun glint (Figure 18, Figure 19). Very few pixels were removed in the glint filtering process for each of these dates, and the resulting imagery had limited streaking. As such, I could use the entire ground truth dataset ( $N = 51$ ) for each of these dates to inform the classifications. The August 1 and August 18 flights both had a maximum sun angle below  $52^\circ$  (Table 5) which seems to have reduced the amount of sun glint in the imagery (Figure 18, Figure 19). In contrast, the June 7 and June 23 flights which I did not use in my analysis because there was too much glint had maximum sun angles of  $63^\circ$  and  $64^\circ$ , respectively (Figure 15-16, Table 5).

I prioritized flying during the lowest low tides of the season, but given the quality of the imagery, it seems that striking a balance between tide and sun angle is necessary to produce high-quality imagery of eelgrass in Padilla Bay. Sun glint is exacerbated in shallow waters lacking eelgrass because the water readily forms wind-blown waves. As a result, I'd suggest flying only when speeds are below  $5 \text{ m s}^{-1}$ . Furthermore, to keep imagery consistent within each flight, operators should note when wind speeds change over the course of a flight, even if under  $5 \text{ m s}^{-1}$  since waves can form in shallow waters even under low wind speeds, resulting in sun glint. In addition to this, the lowest low tides often coincide with high sun angles (Table 5). For example, the minimum tides for the June 7, June 23, July 4, and July 21 flights were all lower than -2.0 ft below MLLW and each of these dates had a maximum sun angle greater than  $60^\circ$  (Table 5). These dates were all heavily impacted by sun glint and were either excluded from analysis or cropped to a smaller area to avoid glint impact. Thus, putting less emphasis on flying during the lowest low tides in Padilla Bay and placing more emphasis on flying at a lower sun

angle ( $< 52^\circ$ ) and at wind speeds  $< 5 \text{ m s}^{-1}$  should reduce the interference of sun glint in UAS imagery.

In order to monitor seasonal dynamics during future monitoring efforts, it will be crucial to keep the flight conditions as consistent as possible, so the resulting imagery is consistent between collection dates. It is possible to schedule flights from April to August where the minimum tide is approximately -1.9 ft below MLLW and the maximum sun angle is around  $52^\circ$ , which were the parameters met for the August 1 and August 18 flights which produced the highest quality imagery (Table 6). These criteria should be taken into consideration when planning UAS flights over Padilla Bay and would likely be of use in other shallow eelgrass meadows.

#### 4.2 | Impact of epiphyte load

Given that epiphytes on eelgrass have been known to consist of over half the biomass in some meadows, seasonal variation in epiphyte biomass could introduce a source of noise in the spectral signatures of *Z. japonica* and *Z. marina* (Sieburth and Thomas 1973, Ruesink 2016). Previous studies in Padilla Bay indicated that epiphytes on eelgrass do vary seasonally and have their highest biomass in spring and summer (Whiting 1983, Thom 1990). However, I found that epiphyte biomass in my study area was generally below 50% of the plant biomass. Also, I did not observe any significant seasonal variation in epiphyte load as a percentage of total plant biomass for either *Z. japonica* or *Z. marina* (Figure 5). Since my study was conducted in the summer from June through August, I may have missed the early season increase in epiphyte load. Although seasonal variation in epiphyte load was not an issue for my study, any future studies that begin early in the spring will need to consider the impact of seasonal variation in epiphyte load on spectral signatures.

While I did not observe any significant seasonal variation in epiphyte load from July to September, the variance of epiphyte load among sample sites for any given date was high (Figure 5). This indicates that there may be spatial variation in epiphyte load as opposed to temporal variation in epiphyte load during the summer months. Overall, I did not observe any notable spatial variation in epiphyte load as a function of elevation above MLLW (Figure 6). However, there was a stronger relationship between epiphyte load and elevation above MLLW for *Z. marina* samples collected in August ( $R^2 = 0.63$ , Figure 7). Increasing epiphyte load with increasing depth was also observed by Thom (1990) where net primary productivity in epiphytes increased from a depth of 0.8 m above MLLW to -0.1 m below MLLW. Also, the August 1 and August 18 classifications were arguably the best for each of the segmentation techniques which may be an indicator that epiphyte load is a spectral predictor of eelgrass species when it is positively correlated with depth (Figure 9-12). However, the August 1 and August 18 imagery was also the highest quality imagery collected in this study, and without additional investigation it is impossible to conclude whether epiphyte load affects the spectral signature of eelgrass from my results. I did not collect the data necessary to rigorously evaluate this claim but doing so would provide interesting opportunities for future research. Furthermore, determining whether spatial variation in epiphyte load produces a significant amount of noise in the spectral data could help efforts to refine delineation between *Z. marina* and *Z. japonica* in modeling efforts.

#### 4.3 | Principal components analysis

##### 4.3.1 | Brightness index

The consistent negative loadings for all bands of PC1 of the full season analysis and PC2 for the July 4 analysis indicate that these PCs are essentially indices of overall brightness. It is noteworthy that this brightness index captures most of the variance (61%) in the full season

analysis but only 33% for the July 4 analysis (Table 7, Table 8). This probably results from large brightness variance resulting from illumination differences and sun glint between the different image dates that were included in the full season analysis. These illumination differences result from variation in sun angle and cloud cover between dates.

#### 4.3.2 | Vegetation index

The main plant pigments of chlorophyll *a*, chlorophyll *b*,  $\alpha$ -carotene, and lutein all absorb strongly in the blue and red portions of the visible spectrum. High reflectance in the NIR results from the absence of absorption in this portion of the spectrum and strong scattering and reflectance by leaf mesophyll cells within the leaf (Gates et al. 1965, Tucker and Garratt 1977). Contrasting loadings for the red edge and NIR bands vs. the red and blue bands for PC2 of the full season analysis (Table 7) and for PC1 of the July 4 analysis (Table 8) indicate that these PCs represent a vegetation index. In particular, the contrasting loadings for the red vs. the red edge and NIR bands for these PCs are analogous to the structure/content of the NDVI and NDRE. It is noteworthy that, as noted above, although photosynthetic pigments absorb quite strongly in both the red and blue portion of the spectrum – and actually somewhat more strongly in the blue – the blue portion of the spectrum is not typically used for vegetation remote sensing when using spaceborne sensors. This is due to the effects of Rayleigh scattering, which results in differential scattering of short wavelengths. This scattering is most pronounced when there is a very long pathlength between the sensor and the vegetation, as is the case for spaceborne sensors (Campbell 2007). However, for sensors on a UAV, the pathlength from the sensor to the ground is minimal and this explains why the loadings for the Coastal blue 444(28) and Blue 475(32) bands are comparable to those of the Red 650(16) and Red 668(14) bands for PC2 and PC1 for both the full season and July 4 analyses, respectively. It is also noteworthy that for the July 4

analysis, the PCA-based vegetation index (PC1) captures most of the scene variance (64%; Table 8) while for the full season analysis, the PCA-based brightness index (PC1) captures most of the variance (60%; Table 7).

#### 4.3.3 | PC3

For both the full season and July 4 analyses, interpretation of the loadings for PC3 are less clear than those for PC1 and PC2 and the loadings for PC3 are somewhat different for these two analyses. For both analyses, PC3 captures only a very small proportion of the variation in the imagery (1.6 and 0.7%, respectively). For the full season, there was a contrast of blue and red with green, which mimics the known absorbance curve for vegetation, where blue and red are absorbed strongly while green is reflected (Gates et al. 1965). In the July 4 PCA, there's a strong contrast between the red edge and NIR bands. The red edge is known to relate to chlorophyll content in leaves (Gates et al. 1965) which suggests PC3 could also be a vegetation index. Interestingly, the contrasts in the loadings for the full season and July 4 PCAs are different but relate to the same reflectance trends in plants. Despite the very small proportion of the variance that is explained and the ambiguous meaning of this PC, it was included in the models with the greatest predictive power.

#### 4.4 | Pixel-based models to predict percent eelgrass cover

In an effort to model the percent coverage of eelgrass, I evaluated the use of a variety of linear regression models that were based on individual bands, band combination, common vegetation indices and principal components axes. Overall, the predictive power of the models was quite good with  $R^2$  values for the best models ranging from 0.75 to 0.89 (Table 9). The models created to predict total percent cover of eelgrass in the July 4 imagery consistently outperformed those created for the full season of imagery (Table 9). As previously stated, this is

likely because there is more overall variation in reflectance in the full season between each collection date due to variation in tide stage and sun angle (Table 5) as well as unmeasured factors such as cloud cover and wind speed. Consequently, there was more noise in the data, as evidenced by the brightness index (PC1 for the full season analysis) explaining 61% of the variation for the full season PCA (Table 7) but only 34% of the variation for the July 4 PCA (Table 8).

Overall, the best percent cover model was based on a combination of the Red 650(16) and Red edge 717(12) bands (full season  $R^2 = 0.79$ , July 4  $R^2 = 0.89$ , Table 9). Chlorophyll absorbs strongly in the red part of the spectrum, around 645 nm, which is captured by the Red 650(16) band of the Micasense camera (Gates et al. 1965). Gates et al. (1965) were among the first to suggest that the position of the sharp increase in reflectance in the transition from red to near infrared, known as the red edge, could be useful in measuring chlorophyll content. Furthermore, Delegido et al. (2013) found that using a red band of 674 nm and red edge band of 712 nm in a normalized difference index correlated strongly with the leaf area index in many crop species. The normalized difference index suggested by Delegido et al. (2013) is similar to the standard NDVI but substitutes the red edge band for the NIR band that is typically used for calculating NDVI.

Total percent cover models based on NDVI were nearly as good as the Red 650(16)/ Red edge 717(12) models (full season  $NDVI_{5,10} R^2 = 0.76$ ; July 4  $NDVI_{6,10} R^2 = 0.87$ , Table 9). The PCA -based models were also reasonably good. It is not surprising that the PCA-based vegetation index – PC2 for the full season and PC1 for the July 4 analysis – individually have more predictive power than the other two PCs (Table 8). It is also noteworthy that for the July 4 analysis, where the brightness index (PC2) captures less of the variance in the image, the



vegetation index (PC1) has more predictive power individually ( $R^2 = 0.86$ ) than is the case for the full season analysis where the vegetation index (PC2) has somewhat less predictive power ( $R^2 = 0.61$ ). As noted above, although interpretation of PC3 is not at all clear, it is interesting that it is included in best PCA-based percent cover models for both the full season and July 4 analyses (Table 8). In the case of the full season analysis, using the brightness index (PC1) and vegetation index (PC2) is the next best model with an  $R^2$  of 0.71 but the model that includes PC3 increases the predictive power to 0.75. For the July 4 analysis only the vegetation index (PC1) and PC3 are included in the best model, with an  $R^2$  of 0.887 and the addition of the brightness index (PC2) reduces the predictive power of the model very slightly to 0.885. Again, it is not at all clear whether PC3 is really picking up on a true signal in the data or if this simply represents a spurious result.

Predicting cover of *Z. japonica* and *Z. marina* individually proved to be a challenge for the pixel-based analysis. The  $R^2$  for all the *Z. japonica* regression models were below 0.33 for the full season and below 0.21 for the July 4 data (Table 11). Predicting *Z. marina* cover was a bit more successful, but the best  $R^2$  was 0.56 for the regression using the NDVI<sub>5,10</sub> (Table 12). Using pixel-based methods to predict percent cover of *Z. japonica* and *Z. marina* was ultimately unsuccessful.

#### 4.5 | Object-based image segmentation

Using object-based image segmentation to define areas of high *Z. japonica* cover and high *Z. marina* cover yielded promising results. Using SVM with k-fold cross validation on a training and test set with discrete categories produced overall accuracies between 60-78%, which was much more accurate than the pixel-based modeling attempts for each species (Table 15). As evidenced by the pixel-based results, predicting *Z. japonica* cover was a challenge. But, using the

PCA based image segmentation with SVM classification resulted in a user's accuracy of 83.3% and producer's accuracy of 62.5% in identifying *Z. japonica* dominated areas when using only the mean of the first three principal components as predictor variables (Table 15). Identifying *Z. marina* dominated plots was similarly accurate, with a user's accuracy of 65.9% and producer's accuracy of 78.4% for the same method (Table 15). In terms of overall accuracy, the classification which used the 10 band means and the 10 band standard deviations performed the best, with an overall accuracy of 78.3% (Table 15). However, using 20 parameters requires an ample ground truth dataset, which may not be feasible to collect for a smaller study (temporally or spatially). Furthermore, the segmentation based on NDRE was comparable to that of the PCA segmentation (Table 14). But the PCA-based segmentation drastically outperformed the NDRE-based segmentation in correctly classifying *Z. japonica* dominant plots, as the NDRE-based segmentation did not identify any *Z. japonica* plots correctly (Table 15). Thus, the 10-band based segmentation with SVM classification was the most successful in my trials, but the PCA based segmentation is also a good option for picking up on differences between the two eelgrass species and does not require as many predictor variables to obtain a similar result. Using PCA is also a promising method for studies with a multispectral camera with fewer bands. Since many of the contrasts in the loadings were between the red, red edge, and NIR bands, these are the most important to have.

One goal for this study was to evaluate the potential for using spectral signatures to delineate areas of *Z. japonica* and *Z. marina*. The PCA-based segmentation with SVM classification did a good job of accurately classifying areas with over 90% of cover of either species. But there were plenty of plots that were classified as "mixed" that were still dominated one of the species. Although I did attempt to split the mixed category into two more specific

mixed categories: *Z. japonica* dominated mixed and *Z. marina* dominated mixed (Table 13) this resulted in considerable misclassification (Summary: Table 14, Band: Table 21, NDRE: Table 26, NDVI: Table 31, PCA: Table 36). Thus, the best PCA-based segmentation with SVM classification presented here has a broader definition for the mixed category.

The SVM classifications using both means and standard deviations did a better job visually of classifying cover type than the SVM classification based only on means for both the band and PCA informed segmentations (Figure 9-12). Apart from one erroneous swath of *Z. marina* in the southeastern vegetated section of the August 1 imagery, the PCA and band classifications using means and standard deviations follows a general pattern of bare, *Z. japonica* dominated, mixed, and *Z. marina* dominated moving from the coast through the upper and lower intertidal (Figure 9, Figure 12). This also follows the distribution observed by several aerial studies in Padilla Bay as well as annual biomonitoring patterns observed by PB-NERR (Figure 12, Bulthuis 1995, Shull 2000, Table 1). I believe the swath of *Z. marina* in the high intertidal (zone 2) is a result of inconsistent imagery quality across the August 1 flight because *Z. marina* is not dominant at such high elevations (Ruesink et al. 2010). Over the course of the flight, the sun angle increased by over 13° (Table 5), and since flights started at the northeast corner of the study area, the southern portion of the transect was covered by the UAS when the sun angle was highest. For the July 4 and July 21 flights, the impact of the increasing sun angle was so great that transects 2 and 3 were cropped from the orthomosaic.

Interestingly, the segmentation and classification picks up on the presence of two channels in the northern central portion of the study area by classifying them as *Z. marina* dominant (Figure 9, Figure 12). These channels are clearly visible in the raw imagery, especially in the NIR 842(57) band (Figure 18B). Hannam and Wylie-Echeverria (2015) conducted

transplant experiments and found that *Z. marina* outcompeted *Z. japonica* in pools by over 60%. While I do not have the adequate ground truth data needed to validate the presence of *Z. marina* in the channels in my classification, these results would be consistent with the findings of Hannam and Wylie-Echeverria (2015). In their experiments, Hannam and Wylie-Echeverria (2015) also found that *Z. marina* was not prevalent on mounds due to its physiological constraints. Also, some classifications pick up on the mounds in zone 5 at the west end of the transect that are higher than the surrounding area and contain *Z. japonica* and bare areas, even though the zone is primarily intertidal *Z. marina* (Figure 9: 7/21 and 8/1, Figure 12: 7/4, 7/21, 8/1). The fact that these areas show up on some dates and not others may suggest that there are seasonal dynamics between *Z. marina* and *Z. japonica* in this area, but additional ground truth observations would be required to elucidate these subtleties.

Overall, *Z. japonica* extent in this study is under-classified in comparison to previous studies and regional trends of *Z. japonica* expansion in previously unvegetated areas (Bulthuis 1995, Young et al. 2015). I think this comes down to two factors. First, the SVM classification was built to predict cover in fully vegetated areas. When I segmented the imagery in eCognition, I used an NDVI mask to delineate between vegetated and unvegetated regions in the study area. The minimum segment size of 100 pixels (1 m<sup>2</sup>) produced a vector-based map with segments that had adequate information to define them spectrally, while also allowing small patches of eelgrass in the high intertidal to be defined appropriately. Using this method, I was confident that the segments with an NDVI greater than 0.15 were vegetated and needed further analysis to classify between *Z. marina*, *Z. japonica*, and mixed regions. Thus, to train the SVM, I subset my ground truth dataset to only those plots that were at least 80% vegetated. I think this method worked well in terms of classifying thickly vegetated regions, which are primarily mixed and *Z.*

*marina* dominant. It also negates the need for future studies to collect ground truth data for plots that are less than 80% vegetated since the NDVI mask does a good job delineating bare versus vegetated regions.

My ground truth collection was based on plot locations that could contain a thickly vegetated area alongside a bare area, resulting in a low overall percent eelgrass cover (which was likely *Z. japonica*). These plots were excluded from the SVM training because they were not at least 80% vegetated. I maintain that these plots should not have been used to build the SVM in this study, since bare mud has a much different spectral signature than vegetation. Secondly, I defined species dominance as >90% of the total vegetation in a plot that was at least 80% vegetated (Table 13). This rule helped increase the overall accuracy of my segmentation classifications (Table 14), but there were several plots with a high percentage of *Z. japonica* that were regarded as mixed since they did not meet the 90% threshold. I think this approach would benefit from additional *Z. japonica* dominant plots that were at least 80% vegetated in total. This would help define the *Z. japonica* spectral signature more rigorously and improve the overall results. Furthermore, additional ground truth plots would help refine the mixed category. Ideally, there could be several levels of “mixed” depending on the ratio of *Z. japonica* to *Z. marina*. But in this study, I simply did not have enough examples of each potential mixed category to train a robust SVM algorithm that could accurately predict multiple mixed categories.

#### 4.6 | Conclusion

Although sun glint presented challenges throughout this study by limiting the number of orthomosaics in the final dataset and preventing the use of many ground truth data points, I was able to develop and test several models for eelgrass cover estimation in Padilla Bay, Washington. Overall, using one date of imagery instead of a full season’s worth of imagery produced better

results. In the pixel-based analysis, using the red and red edge bands was useful in predicting overall eelgrass cover since reflectance in these bands is indicative of plant structure and health. Similarly, the PCA for the full season and the July 4 data produced a principal component that contrasted the reflectance of the visible spectrum with the red edge and NIR, which mirrors the trends in the reflectance curve for vegetation. This method seems to be a good way to condense imagery data from cameras with many bands, since simply using all bands in linear regression leads to collinearity between predictor variables. But, if delineating between *Z. japonica* and *Z. marina* is of interest, pixel-based efforts are not sufficient. Instead, I found that segmenting based on PCA or the full 10-band dataset of the Micasense Dual Camera both performed well when using segment means and standard deviations as predictor variables in the classification, especially when it came to delineating between *Z. japonica* and *Z. marina* dominated areas, suggesting that further research can continue to define spectral signatures for each of these species.

## 5.0 | Works Cited

- Agisoft LLC. 2020. Agisoft Metashape User Manual, Professional Edition, Version 1.6.  
Available online at [https://www.agisoft.com/pdf/metashape-pro\\_1\\_6\\_en.pdf/](https://www.agisoft.com/pdf/metashape-pro_1_6_en.pdf/) (accessed 8 January 2021).
- Almasi, K. N., and P. M. Eldridge. 2008. A dynamic model of an estuarine invasion by a non-native seagrass. *Estuaries and Coasts* 31:163-176.
- Anderson, K., and K. J. Gaston. 2013. Lightweight unmanned aerial vehicles will revolutionize spatial ecology. *Frontiers in Ecology and the Environment* 11:138-146.
- Baldwin, J. R., and J. R. Lovvorn. 1994. Expansion of seagrass habitat by the exotic *Zostera japonica*, and its use by dabbling ducks and brant in Boundary Bay, British Columbia. *Marine Ecology Press Series* 103:119-127.
- Ball, D., M. Soto-Berelov, and P. Young. 2014. Historical seagrass mapping in Port Phillip Bay, Australia. *Journal of Coastal Conservation* 18:257-272.
- Bando, K. J. 2006. The roles of competition and disturbance in a marine invasion. *Biological Invasions* 8:755-763.
- Barbier, E. B., S. D. Hacker, C. Kennedy, E. W. Koch, A. C. Stier, and B. R. Stillman. 2011. The value of estuarine and coastal ecosystem services. *Ecological Monographs* 81:169-193.
- Berry, H., A. T. Sewell, S. Wyllie-Echeverria, B. Reeves, T. Mumford, J. R. Skalski, R. Zimmerman, and J. Archer. 2003. Puget Sound submerged vegetation monitoring project: 2000–2002 monitoring report. Nearshore Habitat Program, Washington State Department of Natural Resources, Olympia.
- Boardman, F. C., and J. L. Ruesink. 2022. Competition and coexistence in a rare Northeastern Pacific multispecies seagrass bed. *Aquatic Botany* 176:103450

- Bryson, M., M. Johnson-Roberson, R. J. Murphy, and D. Bongiorno. 2013. Kite aerial photography for low-cost, ultra-high spatial resolution multi-spectral mapping of intertidal landscapes. *PLoS One* 8:1-15.
- Bulthuis, D. A. 1995. Distribution of seagrasses in a north Puget-Sound estuary: Padilla Bay, Washington, USA. *Aquatic Botany* 50:99-105.
- Bulthuis, D. A., and S. Shull. 2006. Monitoring the distribution of submerged aquatic vegetation in Padilla Bay, NERR-SWMP Biomonitoring Pilot Site, 2004: Final Report. Washington State Department of Ecology, Mount Vernon.
- Casella, E., A. Collin, D. Harris, S. Ferse, S. Bejarano, V. Parravicini, J. L. Hench, and A. Rovere. 2017. Mapping coral reefs using consumer-grade drones and structure from motion photogrammetry techniques. *Coral Reefs* 36:269-275.
- Campbell, J. B. 2007. *Introduction to Remote Sensing*. The Guilford Press, New York.
- Christiaen, B., P. Dowty, L. Ferrier, J. Gaeckle, H. Berry, J. Stowe, and E. Sutton. 2016. Puget Sound submerged vegetation monitoring program: 2014 Report. Nearshore Habitat Program, Washington State Department of Natural Resources, Olympia.
- Delegido, J., J. Verrelst, C. M. Meza, J. P. Rivera, L. Alonso, and J. Moreno. 2013. A red-edge spectral index for remote sensing estimation of green LAI over agroecosystems. *European Journal of Agronomy* 46:42-52.
- eCognition Developer. 2019. Guided Tours and Tutorial Overview. Trimble Inc. Available online at [https://docs.ecognition.com/v9.5.0/eCognition\\_documentation/Modules/7%20Tutorials/Tutorial%20Overview.htm](https://docs.ecognition.com/v9.5.0/eCognition_documentation/Modules/7%20Tutorials/Tutorial%20Overview.htm) (accessed 2 May 2021).
- Federal Aviation Administration. 2020. Title 14, Chapter I, Subchapter F, Part 107 – Small Unmanned Aircraft Systems. Available online at <https://www.ecfr.gov/cgi-bin/text->



idx?SID=795f3720e106147f41212aef340f0d11&mc=true&node=pt14.2.107&rgn=div5  
(accessed 10 November 2019).

Gates, D. M., H. J. Keegan, J. C. Schleiter, and V. R. Weidner. 1965. Spectral properties of plants. *Applied Optics* 4:11-20.

Hahn, D. R. 2003. Alteration of microbial community composition and changes in decomposition associated with an invasive intertidal macrophyte. *Biological Invasions* 5:45-51.

Hannam, M. P. and S. Wyllie-Echeverria. 2015. Microtopography promotes coexistence of an invasive seagrass and its native congener. *Biological Invasions* 17:381-395.

Hansen, J. C. R. and M. A. Reidenbach. 2013. Seasonal growth and senescence of a *Zostera marina* seagrass meadow alters wave-dominated flow and sediment suspension within a coastal bay. *Estuaries and Coasts* 36:1099-1114.

Harrison, P. G. 1982. Comparative growth of *Zostera japonica* Aschers. & Graebn, and *Z. marina* L. under simulated intertidal and subtidal conditions. *Aquatic Botany* 14:373-379.

Harrison, P. G. and R. E. Bigley. 1982. The recent introduction of the seagrass *Zostera japonica* Aschers. and Graebn. to the Pacific Coast of North America. *Canadian Journal of Fisheries and Aquatic Sciences* 39:1642-1648.

Khan, M. A., Y. H. Fadlallah, and K. G. Al-Hinai. 1992. Thematic mapping of subtidal coastal habitats in the western Arabian Gulf using Landsat TM data – Abu Ali Bay, Saudi Arabia. *International Journal of Remote Sensing* 13:605-614.

Klemas, V. V. 2015. Coastal and environmental remote sensing from unmanned aerial vehicles: an overview. *Journal of Coastal Research* 31:1260-1267.

- Meyer, D., E. Dimitriadou, K. Hornik, A. Weingessel, and F. Leisch. 2021. e1071: Misc Functions of the Department of Statistics, Probability Theory Group (Formerly: E1071), TU Wien. R package version 1.7-9. Available online at <https://CRAN.R-project.org/package=e1071> (accessed 10 October 2021).
- Micasense. RedEdgeMX Dual Camera Imaging System. Available online at <https://micasense.com/dual-camera-system/> (accessed 28 April 2022).
- Nahirnick, N. K., L. Reshitnyk, M. Campbell, M. Hessing-Lewis, M. Costa, J. Yakimishyn, and L. Lee. 2019. Mapping with confidence; delineating seagrass habitats using Unoccupied Aerial Systems (UAS). *Remote Sensing in Ecology and Conservation* 5:121-315.
- Nahirnick, N. K., M. Costa, S. Schroeder, and T. Sharma. 2020. Long-term eelgrass habitat change and associated human impacts on the west coast of Canada. *Journal of Coastal Research* 36:30-40.
- NOAA Tides & Currents. 2020. 9448558 La Conner, Swinomish Slough, WA. Available online at <https://tidesandcurrents.noaa.gov/noaatidepredictions.html?id=9448558/> (accessed 1 March 2020).
- RStudio Team. 2020. RStudio: Integrated Development Environment for R. RStudio, PBC, Boston, MA. Available online at <http://www.rstudio.com/>.
- Rubin, S. P., M. C. Hayes, and E. E. Grossman. 2018. Juvenile Chinook salmon and forage fish use of eelgrass habitats in a diked and channelized Puget Sound river delta. *Marine and Coastal Fisheries* 10:435-451.
- Ruesink, J. L. 2016. Epiphyte load and seagrass performance are decoupled in an estuary with low eutrophication risk. *Journal of Experimental Marine Biology and Ecology* 481:1-8.

- Ruesink, J. L., J. Hong, L. Wisehart, S. D. Hacker, B. R. Dumbauld, M. Hessing-Lewis, and A. C. Trimble. 2010. Congener comparison of native (*Zostera marina*) and introduced (*Z. japonica*) eelgrass at multiple scales within a Pacific Northwest estuary. *Biological Invasions* 12:1773-1789.
- senseFly. Parrot Sequoia+ Multispectral Camera. Available online at <https://www.sensefly.com/camera/parrot-sequoia/> (accessed 30 January 2022).
- Sentera. 6X Multispectral Sensor. Available online at <https://sentera.com/wp-content/uploads/2021/11/6X-Multispectral-Flyer.pdf> (accessed 30 January 2022).
- Shafer, D. J., S. Wyllie-Echeverria, and T. D. Sherman. 2008. The potential role of climate in the distribution and zonation of the introduced seagrass *Zostera japonica* in North America. *Aquatic Botany* 89:297-302.
- Shull, S. 2000. Mapping seagrass meadows of Padilla Bay, Washington, using a 1996 compact airborne spectrographic imager (CASI) dataset. M.S. Thesis, Western Washington University, Bellingham, Washington.
- Sieburth, J. M., and C. D. Thomas. 1973. Fouling on eelgrass (*Zostera marina*). *Journal of Phycology* 9:46-50.
- Thom, R. M. 1990. Spatial and Temporal patterns in plant standing stock and primary production in a temperate seagrass system. *Botanica Marina* 33:497-510.
- Trimble Germany GmbH. 2021. Trimble Documentation eCognition Developer 10.1 User Guide. Trimble Germany GmbH, Munich, Germany.
- Tucker, C. J., and M. W. Garratt. 1977. Leaf optical system modeled as a stochastic process. *Applied Optics* 16:635-642.

- USGS National UAS Project Office. 2017. Unmanned Aircraft Systems Data Post-Processing, Structure-from-Motion Photogrammetry, Section 2- MicaSense 5-band MultiSpectral Imagery. Available at <https://uas.usgs.gov/nupo/pdf/PhotoScanProcessingMicaSenseMar2017.pdf> (accessed 15 March 2020).
- Webber, H. H., T. F. Mumford, and J. Eby. 1987. Remote sensing inventory of the seagrass meadow of the Padilla Bay National Estuarine Research Reserve: Areal extent and estimation of biomass. M.S. Thesis, Western Washington University, Bellingham, WA.
- Whiting, M. C. 1983. Distributional patterns and taxonomic structure of diatom assemblages in Netarts Bay, Oregon. Ph.D. Dissertation, Oregon State University, Corvallis.
- Williams, S. L., and M. H. Ruckelshaus. 1993. Effects of nitrogen availability and herbivory on eelgrass (*Zostera marina*) and epiphytes. *Ecology* 74:904-918.
- Xu, D., B. Chen, B. Shin, X. Wang, Y. Yan, L. Xu, and X. Xin. 2019. The classification of grassland types based on object-based image analysis with multisource data. *Rangeland Ecology & Management* 72:318-326.
- Young, D., P. Clinton, D. Specht, and T. C. M. Collura. 2015. Comparison of non-native dwarf eelgrass (*Zostera japonica*) and native eelgrass (*Zostera marina*) distributions in a northeast Pacific estuary: 1997-2014. *Botanica Marina* 58:239-250.

## **6.0 | Appendices**

### **6.1 | Image processing workflow in Agisoft Metashape**

All image processing was completed in Agisoft Metashape Professional Version 1.6.4 build 10928 (64 bit). The workflow was largely based on instructions published by the United States Geological Survey National Unmanned Aircraft Systems (UAS) Project Office and the Agisoft Helpdesk Portal (USGS National UAS Project Office 2017). Parameters used in constructing orthomosaics for this study are compiled in Table 17.

#### **6.1.1 | Loading imagery and calibrating reflectance**

Photos were added to a new project as part of a multi-camera system, which allows Agisoft Metashape to load the images properly to create a multi-band image. Calibration images taken before the flight were added in this step as well. The “Calibrate Reflectance” tool locates the calibration panel images and moves them to a separate folder. Agisoft automatically applies a mask to cover everything in the image aside from the reflectance panel. Next, I input the calibration information for the calibration panel. This consists of a list of reflectance by wavelength that is specific to this calibration panel. This information was acquired directly from Micasense. Additional calibration information is provided by a sun sensor that is mounted on the top of the drone and that is linked to the camera. The sun sensor records incoming illumination in real time and stores this information with each image. The final pre-processing step is to use the reflectance panels and data from the sun sensor to run the reflectance calibration. This process corrects for variation in illumination that results from variation in cloud cover, haze and sun angle and results in images with actual reflectance values for each image rather than simply a brightness index.

### 6.1.2 | Aligning photos

In this process, exterior and interior orientation parameters are estimated based on translation components, rotation angles, and camera configuration (Agisoft LLC 2020). The result is a sparse point cloud which contains the locations of matched tie points between images. The parameters for the “Align Photos” tool were set based on the method outlined by Agisoft for use with a Micasense sensor (Table 17, USGS National UAS Project Office 2017). Due to the large size of the imagery dataset, accuracy for the “Align Photos” tool was set to “medium”. This downsizes the images by a factor of 4 during the initial alignment which speeds up processing time. I ran the alignment with “Generic Preselection” and “Reference Preselection”, both of which use spatial metadata from the images to determine which images overlap. The generic preselection tool subsets the overlapping images and matches them with a lower accuracy setting. Reference preselection uses coordinate information stored with each image to determine overlapping images and is useful for more uniform scenes, such as the eelgrass meadows captured in this study. The key point limit was set to 40,000, which is the maximum number of features in each image to be considered during the alignment. The tie point limit was set to 4,000, which is the maximum number of matching points between any two images.

While processing the imagery for some data collection dates, not all photos could be aligned at medium accuracy. When this occurred, I subset the unaligned photos and ran the “Align Photos” tool with all the same parameters except the accuracy was set to “low”. This process was repeated with accuracy set to “lowest” if there were remaining unaligned cameras. Once the alignment was complete, I ran the “Optimize Cameras” tool using the fit f, cx, cy, k1, k2, k3, b1, b2, p1, and p2 parameters.

Table 17. Parameters and settings used in Agisoft Metashape to align photos, reduce errors, and build the dense point cloud, mesh, DEM, and orthomosaic layers. Settings used were kept consistent between imagery dates, except for the Gradual Selection settings. These levels were set depending on the total number of points selected, as per the USGS UAS Project Office guidelines.

<b>Tool</b>	<b>Parameter</b>	<b>Setting used</b>
<b>Align Photos</b>	<b>Accuracy</b>	Medium
	<b>Generic preselection</b>	Checked
	<b>Reference preselection</b>	Checked
	<b>Key point limit</b>	40,000
	<b>Tie point limit</b>	4,000
	<b>Apply masks to</b>	None
	<b>Guided image matching</b>	Unchecked
<b>Gradual Selection</b>	<b>Adaptive camera model fitting</b>	Unchecked
	<b>Reconstruction uncertainty</b>	< level 50, goal = level 10
	<b>Projection accuracy</b>	Set to level where 50% of points are selected
<b>Build Dense Point Cloud</b>	<b>Reprojection error</b>	Set to level where 10% of points are selected
	<b>Quality</b>	Medium
	<b>Depth filtering</b>	Mild
<b>Build Mesh</b>	<b>Calculate point colors</b>	Checked
	<b>Source data</b>	Dense cloud
	<b>Surface type</b>	Height field
	<b>Face count</b>	High
	<b>Interpolation</b>	Enabled
<b>Build DEM</b>	<b>Calculate vertex colors</b>	Checked
	<b>Projection</b>	NAD83 (2011)/ Zone 10N (EPSG::6339)
	<b>Source data</b>	Dense cloud
<b>Build Orthomosaic</b>	<b>Interpolation</b>	Enabled
	<b>Projection</b>	NAD83 (2011)/ Zone 10N (EPSG::6339)
	<b>Surface</b>	Mesh
	<b>Blending mode</b>	Mosaic
	<b>Enable hole filling</b>	Checked
	<b>Pixel size (m)</b>	0.1 x, 0.1 y

### 6.1.3 | Error reduction

The same ground control points were used for all flights (Table 18). I added ground control coordinates as a text file to the project and designated point name, longitude, latitude, and elevation (m). Once points were created, I subset images to those that contained ground control points. I manually shifted the position of the markers in Agisoft to match the location of the ground control panel in the imagery. This adjusts the overall photo alignment to the ground control points.

After georeferencing the ground control panels, I filtered points as recommended by the USGS National UAS Project Office (Table 19, USGS National UAS Project Office 2017). Using the "Gradual Selection" tool, I removed points based on their values for several criterion, including reconstruction uncertainty, projection accuracy, and reprojection error. The degree to which points were filtered varied based on the specific image set, but overall, parameters described by the USGS National UAS Project Office were used (Table 17). After deleting points in each step, I optimized cameras using the fit  $f$ ,  $c_x$ ,  $c_y$ ,  $k_1$ ,  $k_2$ ,  $k_3$ ,  $p_1$ , and  $p_2$  parameters. After the gradual selection steps, I tightened the tie point accuracy to 0.7. This value was chosen based on the clarity of the imagery.

After all error reduction steps were complete, I ran the "Optimize Cameras" tool again, using the fit  $f$ ,  $c_x$ ,  $c_y$ ,  $k_1$ ,  $k_2$ ,  $k_3$ ,  $k_4$ ,  $b_1$ ,  $b_2$ ,  $p_1$ ,  $p_2$ ,  $p_3$ , and  $p_4$  parameters.



Table 18. List of plots used as ground control points for orthomosaic georectification. All points have highly accurate RTK coordinates.

<b>Transect #</b>	<b>Zone 1</b>	<b>Zone 2</b>	<b>Zone 3</b>	<b>Zone 4</b>	<b>Zone 5</b>
1	1.1.E	1.2.G	1.3.C	1.4.A	1.5.B 1.5.C
			1.3.D	1.4.E	
			1.3.F	1.4.G	
			1.3.H	1.4.I	
			1.3.J	1.4.K	
3	3.1.D 3.1.G	3.2.B	3.3.A	3.4.A 3.4.B 3.4.G	
		3.2.C	3.3.C		
		3.2.D	3.3.D		
		3.2.G	3.3.E		
			3.3.G		

Table 19. Summary of parameters used for error reduction and point filtering on sparse point cloud in Agisoft Metashape Professional 1.6.4.

<b>Parameter</b>	<b>Purpose</b>
Reconstruction uncertainty	Remove points with poor geometry
Projection accuracy	Remove points with pixel matching errors
Reprojection error	Remove points with pixel residual errors

#### 6.1.4 | Building the dense point cloud, mesh, digital elevation model, and orthomosaic

Next, the sparse point cloud created from the photo alignment is used to generate a dense point cloud of the study area. The dense point cloud is based on depth maps which are calculated using dense stereo matching (Agisoft LLC 2020). In Agisoft Metashape Professional Version 1.6.4, each point in the dense point cloud has a confidence value calculated by the number of contributing depth maps used to locate that point. Parameters used to calculate the dense point cloud were based in part on suggestions by Agisoft and in part on user decision (Table 17). Overall quality was set to “medium” to strike a balance between detail and processing time. Depth filtering, a tool used to identify outliers, was set to “mild”. According to Agisoft, “mild”

depth filtering is recommended for scenes in which there are important small details. Since one goal of this study is to evaluate the eelgrass to the finest degree possible with UAS, using “mild” depth filtering seemed appropriate. Finally, “calculate point colors” was checked.

I used the dense point cloud to construct a polygonal mesh. This layer is based on the depth maps data calculated in the dense point cloud creation. Parameters for this tool were chosen based on suggestions by the USGS National UAS Project Office (Table 17, USGS National UAS Project Office 2017). I used the dense point cloud as the source data to generate a higher quality output than would be created if using the sparse point cloud. The “height field” surface type is used for terrain modeling and was selected for this study. Face count was set to “high” which produces the highest detail polygonal mesh. I enabled interpolation so that erroneous holes would be filled during the mesh creation. Finally, I checked “calculate vertex colors” so that the resulting mesh could be viewed in true color. All other parameters were left in their default setting.

To build the digital elevation model (DEM), I used the dense point cloud as the source data. I enabled interpolation which allows the program to calculate the DEM for all areas in the study range with at least one image. I set the projection type as NAD83 (2011)/UTM Zone 10N (EPSG::6339). This projection was used for DEMs on all imagery collection dates. Resolution (m) and total size (pix) were left in their default settings. The DEMs produced were not used for analysis in this study.

The final step in Agisoft Metashape was to create the orthomosaics of the study area. Initially, I built the orthomosaics with the original resolution captured by the Micasense camera, which was 6 cm per pixel. However, the fine original resolution did not warrant the file size and processing time required to create the orthomosaic. Consequently, I resampled the orthomosaic

to a 10 cm per pixel resolution. I built the orthomosaic from the mesh created in earlier steps and set the projection type to NAD83 (2011)/UTM Zone 10N (EPSG::6339). At this point, the initial processing of the imagery in Agisoft Metashape is complete.

## 6.2 | Parameters used in ENVI workflow for PCA

The parameters listed in Table 20 were used in ENVI to produce the full season, July 4, Sentera, and Sequoia PCAs mentioned in this study.

Table 20. Summary of parameters used for PCA in ENVI.

<b>Parameter</b>	<b>Setting used</b>
Spectral subset	10/10 bands
Mask band	Mask data ignore values [all bands]
Stats x and y resize factor	1
Calculate using	Covariance matrix
Output mask value	0
Output data type	Float
Number of PC output bands	10

### 6.3 | Imagery

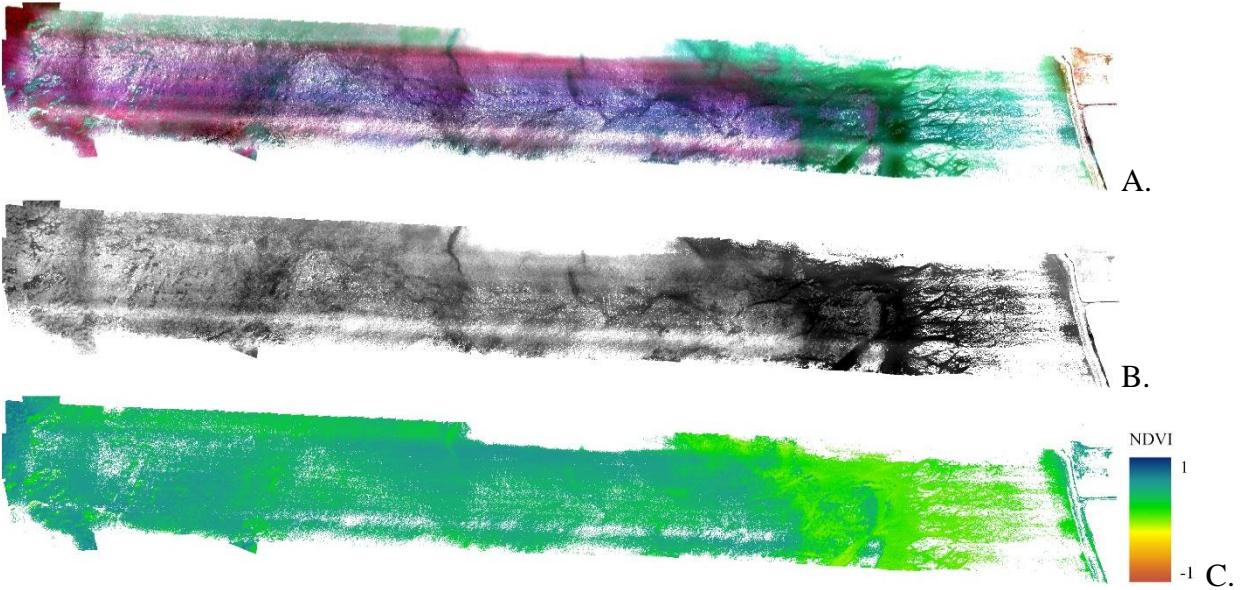


Figure 14. Orthomosaics created from imagery collected on June 7, 2020 in A) color infrared (bands 10, 6, 4), B) infrared (band 10), and C) NDVI.



Figure 15. Orthomosaics created from imagery collected on June 23, 2020 in A) color infrared (bands 10, 6, 4), B) infrared (band 10), and C) NDVI.

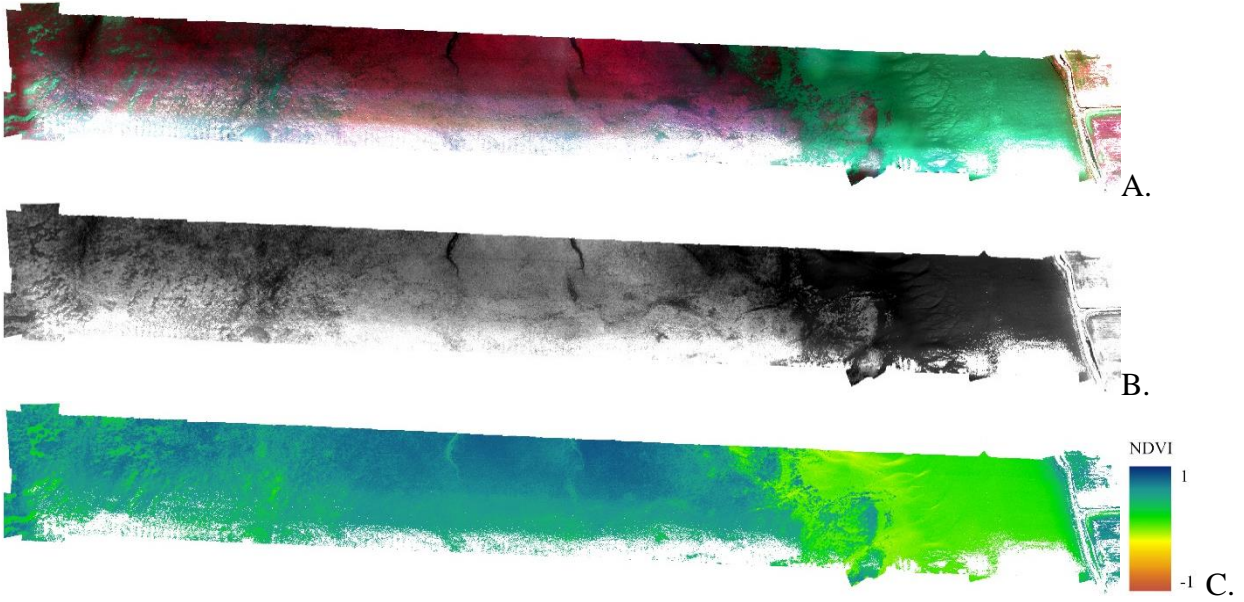


Figure 16. Orthomosaics created from imagery collected on July 4, 2020 in A) color infrared (bands 10, 6, 4), B) infrared (band 10), and C) NDVI.

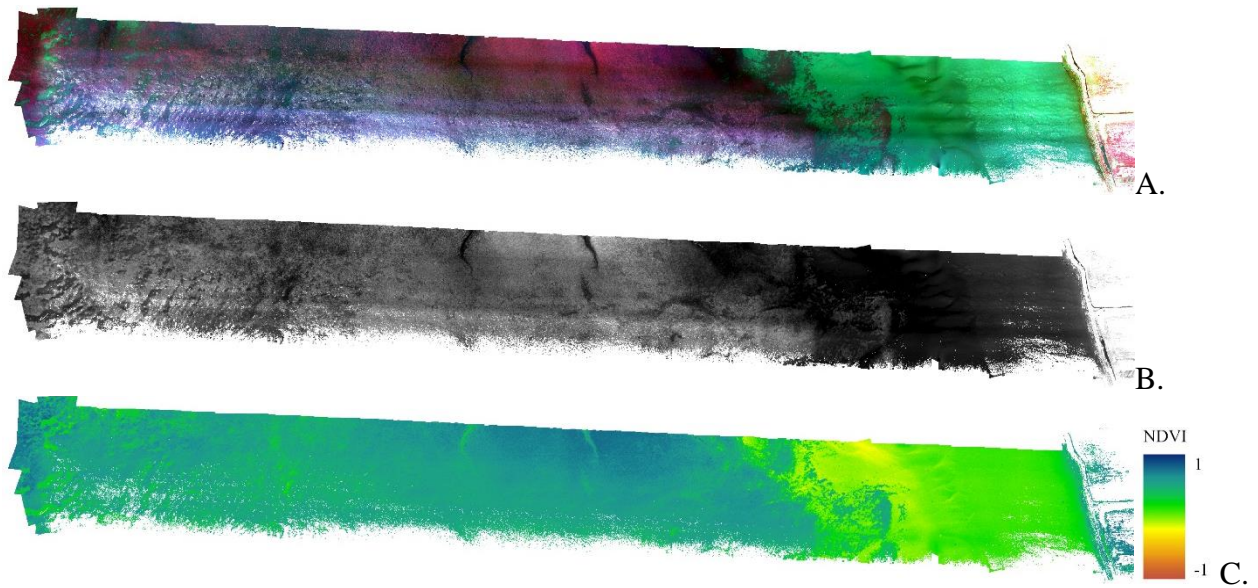


Figure 17. Orthomosaics created from imagery collected on July 21, 2020 in A) color infrared (bands 10, 6, 4), B) infrared (band 10), and C) NDVI.



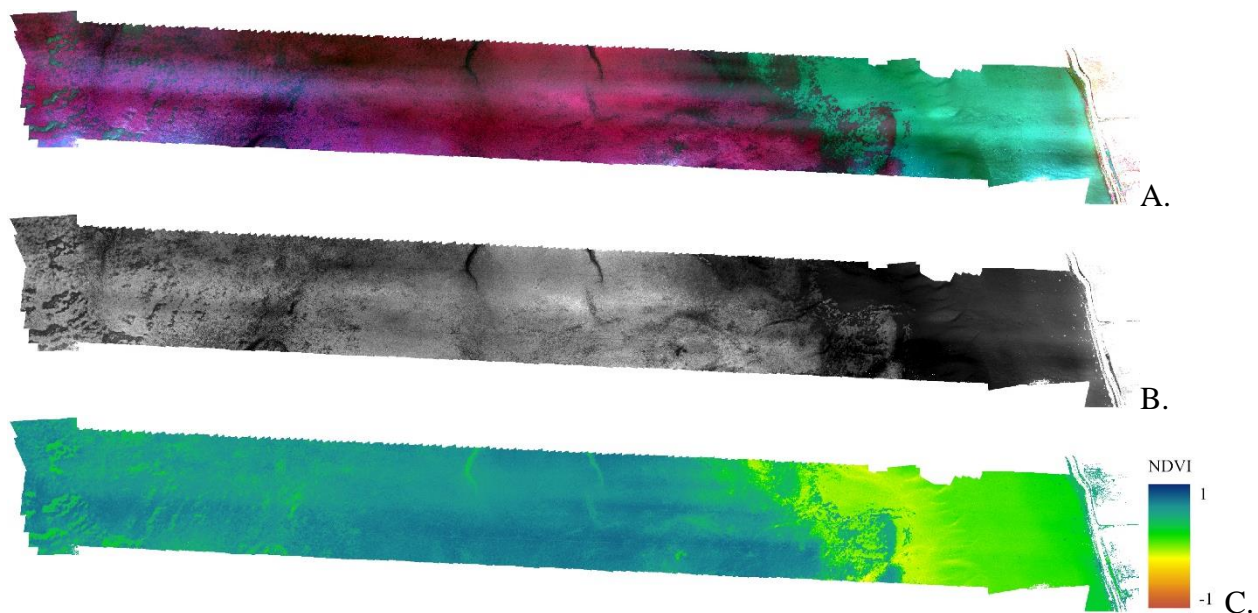


Figure 18. Orthomosaics created from imagery collected on August 1, 2020 in A) color infrared (bands 10, 6, 4), B) infrared (band 10), and C) NDVI.

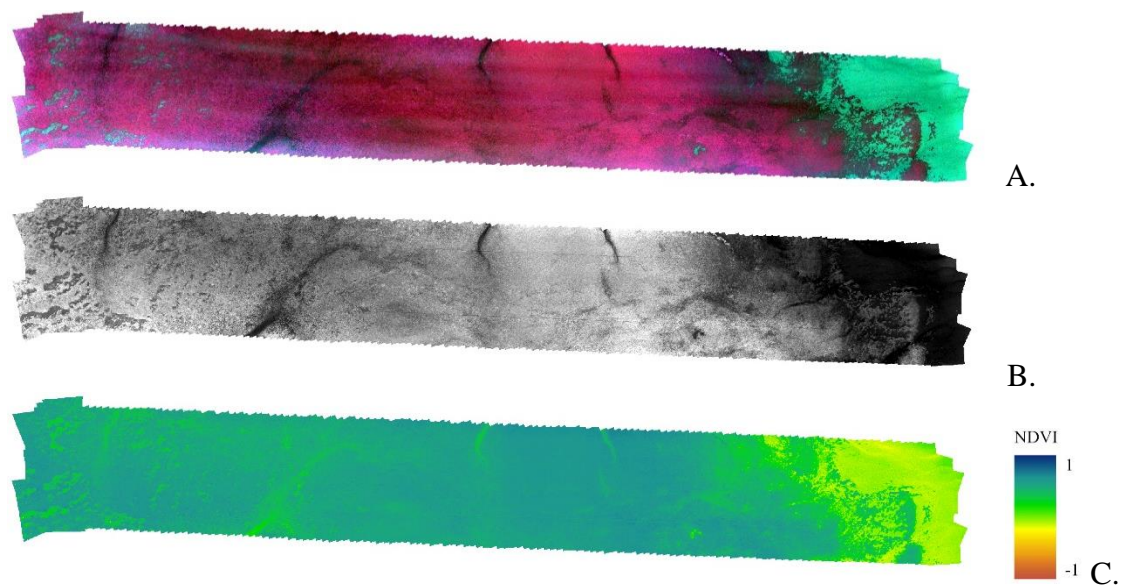


Figure 19. Orthomosaics created from imagery collected on August 18, 2020 in A) color infrared (bands 10, 6, 4), B) infrared (band 10), and C) NDVI. Due to poor image quality in the eastern section of the study area, Agisoft Metashape was not able to stitch together most of the bare area between the coastline and eelgrass beds, resulting in a shorter orthomosaic.

## 6.4 | Object-based image analysis supplemental results

Confusion matrices for all classification methods for all segmentation types are presented in this section. Refer to Table 12 for criteria used to categorize ground truth plots prior to SVM classification.

### 6.4.1 | Band segmentation

Table 21. Accuracy assessment for SVM classification model based on 10 raw band means derived from image segmentation using ground truth categorization method 1. Overall accuracy for this classification method is 57.8%.

		Predicted cover				Row total	Producer's accuracy (%)
		<i>Z. japonica</i> dominant	<i>Z. marina</i> dominant	Mixed, <i>Z. japonica</i> dominant	Mixed, <i>Z. marina</i> dominant		
Actual cover	<i>Z. japonica</i> dominant	4	4	0	0	8	50.0
	<i>Z. marina</i> dominant	0	44	0	0	44	100.0
	Mixed, <i>Z. japonica</i> dominant	0	18	0	0	18	0.0
	Mixed, <i>Z. marina</i> dominant	0	13	0	0	13	0.0
	Column total	4	79	0	0	83	
User's accuracy (%)		100.0	55.7	NA	NA	Total accuracy: 57.8%	

Table 22. Accuracy assessment for SVM classification model based on 10 raw band means derived from image segmentation using ground truth categorization method 2. Overall accuracy for this classification method is 60.2%.

Actual cover	Predicted cover			Row total	Producer's accuracy (%)	
	Z. japonica dominant	Z. marina dominant	Mixed			
	Z. japonica dominant	4	3	1	8	50.0
	Z. marina dominant	0	37	7	44	84.1
	Mixed	0	22	9	31	29.0
Column total	4	62	17	83		
User's accuracy (%)	100.0	59.7	52.9	Total accuracy: 60.2%		

Table 23. Accuracy assessment for SVM classification model based on 10 raw band means derived from image segmentation using ground truth categorization method 3. Overall accuracy for this classification method is 60.2%.

		Predicted cover			Row total	Producer's accuracy (%)
		Z. japonica dominant	Z. marina dominant	Mixed		
Actual cover	Z. japonica dominant	4	3	0	7	57.1
	Z. marina dominant	0	24	13	37	64.9
	Mixed	0	17	22	39	56.4
	Column total	4	44	35	83	
User's accuracy (%)		100.0	54.5	62.9	Total accuracy: 60.2%	



Table 24. Accuracy assessment for SVM classification model based on 10 raw band means and 10 raw band standard deviations derived from image segmentation using ground truth categorization method 3. Overall accuracy for this classification method is 78.3%.

Actual cover	Predicted cover			Row total	Producer's accuracy (%)	
	<i>Z. japonica</i> dominant	<i>Z. marina</i> dominant	Mixed			
	<i>Z. japonica</i> dominant	5	0	2	7	71.4
	<i>Z. marina</i> dominant	0	28	9	37	75.7
	Mixed	0	7	32	39	82.1
Column total	5	35	43	83		
User's accuracy (%)	100.0	80.0	74.4	Total accuracy: 78.3%		

Table 25. Accuracy assessment for SVM classification model based on 10 raw band means derived from image segmentation using ground truth categorization method 4. Overall accuracy for this classification method is 57.8%.

Actual cover	Predicted cover			Row total	Producer's accuracy (%)	
	Z. japonica dominant	Z. marina dominant	Mixed			
	Z. japonica dominant	1	8	2	11	9.1
	Z. marina dominant	0	41	4	45	91.1
	Mixed	0	21	6	27	22.2
Column total	1	70	12	83		
User's accuracy (%)	100.0	58.6	50.0	Total accuracy: 57.8%		

#### 6.4.2 | NDRE segmentation

Table 26. Accuracy assessment for SVM classification model based on the mean and standard deviation of NDRE calculated with red edge 705(10) derived from image segmentation using ground truth categorization method 1. Overall accuracy for this classification method is 55.6%.

		Predicted cover				Row total	Producer's accuracy (%)
		Z. japonica dominant	Z. marina dominant	Mixed, Z. japonica dominant	Mixed, Z. marina dominant		
Actual cover	Z. japonica dominant	0	8	1	1	19	0.0
	Z. marina dominant	0	39	1	5	45	86.7
	Mixed, Z. japonica dominant	0	9	1	4	14	7.1
	Mixed, Z. marina dominant	0	5	2	5	12	41.7
	Column total	0	61	5	15	81	
User's accuracy (%)		NA	63.9	20.0	33.3	Total accuracy: 55.6%	

Table 27. Accuracy assessment for SVM classification model based on the mean and standard deviation of NDRE calculated with red edge 705(10) derived from image segmentation using ground truth categorization method 2. Overall accuracy for this classification method is 63.0%.

		Predicted cover				
		<i>Z. japonica</i> dominant	<i>Z. marina</i> dominant	Mixed	Row total	Producer's accuracy (%)
Actual cover	<i>Z. japonica</i> dominant	0	8	2	10	0.0
	<i>Z. marina</i> dominant	0	36	9	45	80.0
	Mixed	0	11	15	26	57.7
	Column total	0	55	26	81	
User's accuracy (%)		NA	65.5	57.7	Total accuracy: 63.0%	

Table 28. Accuracy assessment for SVM classification model based on the mean NDRE calculated with red edge 705(10) derived from image segmentation using ground truth categorization method 3. Overall accuracy for this classification method is 70.4%.

Actual cover	Predicted cover			Row total	Producer's accuracy (%)	
	<i>Z. japonica</i> dominant	<i>Z. marina</i> dominant	Mixed			
	<i>Z. japonica</i> dominant	0	8	0	8	0.0
	<i>Z. marina</i> dominant	0	32	5	37	86.5
	Mixed	0	11	25	36	69.4
Column total	0	51	30	81		
User's accuracy (%)	NA	62.7	83.3	Total accuracy: 70.4%		

Table 29. Accuracy assessment for SVM classification model based on the mean and standard deviation of NDRE calculated with red edge 705(10) derived from image segmentation using ground truth categorization method 3. Overall accuracy for this classification method is 69.1%.

		Predicted cover			Row total	Producer's accuracy (%)
		<i>Z. japonica</i> dominant	<i>Z. marina</i> dominant	Mixed		
Actual cover	<i>Z. japonica</i> dominant	0	8	0	8	0.0
	<i>Z. marina</i> dominant	0	29	8	37	78.4
	Mixed	0	9	27	36	75.0
	Column total	0	46	35	81	
User's accuracy (%)		NA	63.0	77.1	Total accuracy: 69.1%	

Table 30. Accuracy assessment for SVM classification model based on the mean and standard deviation of NDRE calculated with red edge 705(10) derived from image segmentation using ground truth categorization method 4. Overall accuracy for this classification method is 69.1%.

<u>Actual cover</u>	<u>Predicted cover</u>			Row total	<b>Producer's accuracy (%)</b>	
	<i>Z. japonica</i> dominant	<i>Z. marina</i> dominant	Mixed			
	<i>Z. japonica</i> dominant	0	9	3	12	0.0
	<i>Z. marina</i> dominant	0	42	4	46	91.3
	Mixed	0	9	14	23	60.9
Column total	0	60	21	81		
<b>User's accuracy (%)</b>	NA	70.0	66.7	<b>Total accuracy: 69.1%</b>		

#### 6.4.3 | NDVI segmentation

Table 31. Accuracy assessment for SVM classification model based on the mean and standard deviation of NDVI calculated with red 668(14) derived from image segmentation using ground truth categorization method 1. Overall accuracy for this classification method is 51.3%.

		Predicted cover				Row total	Producer's accuracy (%)
		<i>Z. japonica</i> dominant	<i>Z. marina</i> dominant	Mixed, <i>Z. japonica</i> dominant	Mixed, <i>Z. marina</i> dominant		
Actual cover	<i>Z. japonica</i> dominant	0	10	0	0	10	0.0
	<i>Z. marina</i> dominant	1	40	0	1	42	95.2
	Mixed, <i>Z. japonica</i> dominant	0	16	0	0	16	0.0
	Mixed, <i>Z. marina</i> dominant	0	10	0	0	10	0.0
	Column total	1	76	0	1	78	
User's accuracy (%)		0.0	52.6	NA	0.0	Total accuracy: 51.3%	

Table 32. Accuracy assessment for SVM classification model based on the mean and standard deviation of NDVI calculated with red 668(14) derived from image segmentation using ground truth categorization method 2. Overall accuracy for this classification method is 57.7%.

<u>Actual cover</u>	<u>Predicted cover</u>			Row total	<b>Producer's accuracy (%)</b>	
	<i>Z. japonica</i> dominant	<i>Z. marina</i> dominant	Mixed			
	<i>Z. japonica</i> dominant	0	8	2	10	0.0
	<i>Z. marina</i> dominant	1	28	13	42	66.7
	Mixed	0	9	17	26	65.4
Column total	1	45	32	78		
<b>User's accuracy (%)</b>	0.0	62.2	53.1	<b>Total accuracy: 57.7%</b>		

Table 33. Accuracy assessment for SVM classification model based on the mean NDVI calculated with red 668(14) derived from image segmentation using ground truth categorization method 3. Overall accuracy for this classification method is 64.1%.

		Predicted cover			Row total	Producer's accuracy (%)
		Z. japonica dominant	Z. marina dominant	Mixed		
Actual cover	Z. japonica dominant	2	6	0	8	25.0
	Z. marina dominant	0	31	4	35	88.6
	Mixed	0	18	17	35	48.6
	Column total	2	55	21	78	
User's accuracy (%)		100.0	56.4	80.9	Total accuracy: 64.1%	

Table 34. Accuracy assessment for SVM classification model based on the mean and standard deviation of NDVI calculated with red 668(14) derived from image segmentation using ground truth categorization method 3. Overall accuracy for this classification method is 64.1%.

Actual cover	Predicted cover			Row total	Producer's accuracy (%)	
	<i>Z. japonica</i> dominant	<i>Z. marina</i> dominant	Mixed			
	<i>Z. japonica</i> dominant	2	6	0	8	25.0
	<i>Z. marina</i> dominant	0	22	13	35	62.9
	Mixed	0	9	26	35	74.3
Column total	2	37	39	78		
User's accuracy (%)	100.0	59.5	66.7	Total accuracy: 64.1%		

Table 35. Accuracy assessment for SVM classification model based on the mean and standard deviation of NDVI calculated with red 668(14) derived from image segmentation using ground truth categorization method 4. Overall accuracy for this classification method is 57.7%.

<u>Actual cover</u>	<u>Predicted cover</u>			Row total	<b>Producer's accuracy (%)</b>	
	<i>Z. japonica</i> dominant	<i>Z. marina</i> dominant	Mixed			
	<i>Z. japonica</i> dominant	2	7	3	12	16.7
	<i>Z. marina</i> dominant	0	32	11	43	74.4
	Mixed	0	12	11	23	47.8
Column total	2	51	25	78		
<b>User's accuracy (%)</b>	100.0	62.7	44.0	<b>Total accuracy: 57.7%</b>		

#### 6.4.4 | PCA segmentation

Table 36. Accuracy assessment for SVM classification model based on the means for the first three principal components derived from image segmentation using ground truth categorization method 1. Overall accuracy for this classification method is 58.8%.

		Predicted cover				Row total	Producer's accuracy (%)
		<i>Z. japonica</i> dominant	<i>Z. marina</i> dominant	Mixed, <i>Z. japonica</i> dominant	Mixed, <i>Z. marina</i> dominant		
Actual cover	<i>Z. japonica</i> dominant	5	5	0	0	10	50.0
	<i>Z. marina</i> dominant	0	44	2	0	26	95.6
	Mixed, <i>Z. japonica</i> dominant	0	15	1	1	17	5.9
	Mixed, <i>Z. marina</i> dominant	1	10	1	0	12	0.0
	Column total	6	74	4	1	85	
User's accuracy (%)		83.3	59.5	25.0	0.0	Total accuracy: 58.8%	

Table 37. Accuracy assessment for SVM classification model based on the means for the first three principal components derived from image segmentation using ground truth categorization method 2. Overall accuracy for this classification method is 68.2%.

		Predicted cover			Row total	Producer's accuracy (%)
		Z. japonica dominant	Z. marina dominant	Mixed		
Actual cover	Z. japonica dominant	5	4	1	10	50.0
	Z. marina dominant	0	41	5	46	89.1
	Mixed	1	16	12	29	41.4
	Column total	6	61	18	85	
User's accuracy (%)		83.3	67.2	66.7	Total accuracy: 68.2%	

Table 38. Accuracy assessment for SVM classification model based on the means for the first three principal components derived from image segmentation using ground truth categorization method 3. Overall accuracy for this classification method is 70.6%.

		<u>Predicted cover</u>				
		<i>Z. japonica</i> dominant	<i>Z. marina</i> dominant	Mixed	Row total	<b>Producer's accuracy (%)</b>
<u>Actual cover</u>	<i>Z. japonica</i> dominant	5	2	1	8	62.5
	<i>Z. marina</i> dominant	0	29	8	37	78.4
	Mixed	1	13	26	40	65.0
	Column total	6	44	35	85	
<b>User's accuracy (%)</b>		83.3	65.9	74.3	<b>Total accuracy: 70.6%</b>	

Table 39. Accuracy assessment for SVM classification model based on the means and standard deviations of the first three principal components derived from image segmentation using ground truth categorization method 3. Overall accuracy for this classification method is 70.6%.

		Predicted cover			Row total	Producer's accuracy (%)
		Z. japonica dominant	Z. marina dominant	Mixed		
Actual cover	Z. japonica dominant	6	2	0	8	75.0
	Z. marina dominant	0	27	10	37	73.0
	Mixed	2	11	27	40	67.5
	Column total	8	40	37	85	
User's accuracy (%)		75.0	67.5	73.0	Total accuracy: 70.6%	



Table 40. Accuracy assessment for SVM classification model based on the means for the first three principal components derived from image segmentation using ground truth categorization method 4. Overall accuracy for this classification method is 68.2%.

		<u>Predicted cover</u>				
		<i>Z. japonica</i> dominant	<i>Z. marina</i> dominant	Mixed	Row total	<b>Producer's accuracy (%)</b>
<u>Actual cover</u>	<i>Z. japonica</i> dominant	5	6	1	12	41.7
	<i>Z. marina</i> dominant	0	42	5	47	89.4
	Mixed	2	13	11	26	42.3
	Column total	7	61	17	85	
<b>User's accuracy (%)</b>		71.4	68.9	64.7	<b>Total accuracy: 68.2%</b>	

## 6.5 | Camera comparison

### 6.5.1 | Objective

There are several multispectral sensor options available for research other than the Micasense Dual Camera system, including the five-band Sentera 6X and the four-band Parrot Sequoia (Sentera, senseFly). These cameras are less expensive than the Micasense Dual Camera system but have fewer bands. The goal for this analysis was to determine whether there is a marked difference in the capability to predict percent cover when fewer bands are used to inform the predictions. Band specifications are presented in Table 41.

Table 41. Sentera 6X and Parrot Sequoia band specifications.

<b>Band</b>	<b>Center wavelength (nm)</b>	<b>Band width (nm)</b>
<b>Sentera 6X</b>		
Blue	475	30
Green	550	20
Red	670	30
Red edge	715	10
NIR	840	20
<b>Parrot Sequoia</b>		
Green	550	40
Red	660	40
Red edge	735	10
NIR	790	40

### 6.5.2 | Methods

I compared the efficacy of the Micasense Dual Camera System, Sentera 6X, and Parrot Sequoia cameras by using a subset of the Micasense bands which were closest in wavelength to those of the cameras to conduct additional PCAs. I determined the appropriate bands to use by calculating the wavelength range and overlap for each camera (Table 42). Then, I used the PCA results to inform regression models using the method described in section 2.8.

Table 42. Comparison of bands for the Micasense Dual Camera System, Sentera 6X, and Parrot Sequoia cameras. Overlap refers to percentage of the total width of the Sentera 6X or Parrot Sequoia band covered by the equivalent Micasense band.

<b>Band</b>	<b>Center wavelength (nm)</b>	<b>Band width (nm)</b>	<b>Equivalent Micasense band</b>	<b>Overlap with equivalent Micasense band (%)</b>
Sentera 6X				
Blue	475	30	Blue 475(32)	93.75
Green	550	20	Green 560(27)	50
Red	670	30	Red 668(14)	100
Red edge	715	10	Red edge 717(12)	75
NIR	840	20	NIR 842(57)	20
Parrot Sequoia				
Green	550	40	Green 560(27)	87.04
Red	660	40	Red 650(16) and Red 668(14)*	100
Red edge	735	10	Red edge 740(18)	50
NIR	790	40	NIR 842(57)	0

\*the Parrot Sequoia red band overlapped 100% with each of the Micasense red bands. I calculated the average between these two bands and used the average as the red band layer in the PCA.

### 6.5.3 | Results

Loadings for the Sentera 6X PCA and Parrot Sequoia PCA followed a similar pattern to those of the Micasense PCA. The first principal component consists of loadings in the same direction and of similar magnitudes, indicating its use as a brightness index (Table 43, Table 44). For the Sentera 6X PCA, the second principal component contrasts the blue and red band with the red edge and NIR, which is characteristic of a vegetation index (Table 43). The Parrot Sequoia does not have a blue band, so the second principal component contrasts the green and red with the red edge and the NIR (Table 44). Finally, while the third principal component for each camera explains very little variance in the dataset (2.31 – 2.52%), there are some interesting

patterns. For example, in the Sentera 6X and Parrot Sequoia PCAs, there is a strong positive loading on the green band which highly contrasts the strong negative loadings on the red and NIR bands (Table 43, Table 44).

Table 43. Loadings for the first three principal components of the PCA conducted on a subset of Micasense dual camera bands nearest those of the Sentera 6X camera. The PCA was run on the full season mosaic of imagery (July 4, July 21, August 1, and August 18, 2020).

<b>Band</b>	<b>PC1</b>	<b>PC2</b>	<b>PC3</b>
Blue	0.532941	0.301399	-0.225538
Green	0.573297	-0.034389	0.749426
Red	0.502031	0.357402	-0.448095
Red edge	0.293718	-0.607061	0.036811
NIR	0.221358	-0.641652	-0.430522
<b>% variance explained</b>	56.22	40.26	2.52

Table 44. Loadings for the first three principal components of the PCA conducted on a subset of Micasense dual camera bands nearest those of the Parrot Sequoia camera. The PCA was run on the full season mosaic of imagery (July 4, July 21, August 1, and August 18, 2020). The red band was calculated by averaging both red bands of the Micasense dual camera.

<b>Band</b>	<b>PC1</b>	<b>PC2</b>	<b>PC3</b>
Green	-0.500751	-0.486851	-0.701602
Red	-0.236635	-0.718213	0.644614
Red edge	-0.593288	0.343793	0.038444
NIR	-0.584177	0.359099	0.301247
<b>% variance explained</b>	56.94	40.42	2.31

Overall, the regression models built with the Sentera 6X and Parrot Sequoia PCAs performed very similarly to those built with the Micasense PCA. When predicting total percent cover of eelgrass, the multiple R<sup>2</sup> for the Sentera 6X and Parrot Sequoia were slightly better than the Micasense camera, at 0.766 and 0.774, respectively (Table 45). The regression models for the

Sentera 6X and Parrot Sequoia performed just as poorly as the Micasense camera when predicting *Z. japonica* and *Z. marina* percent cover individually (Table 45).

Table 45. Comparison of multiple linear regression models built to predict total eelgrass percent cover, *Z. japonica* percent cover, and *Z. marina* percent cover. All results are based on the model: percent cover = PC1 + PC2 + PC3. All models are on 3 and 98 degrees of freedom and n=101.

Camera	Multiple R <sup>2</sup>	F statistic	p-value
Micasense	0.7475	100.6	< 0.001
Sentera 6X	0.7658	111.1	< 0.001
Parrot Sequoia	0.7744	116.5	< 0.001
Micasense	0.0458	2.614	0.0555
Sentera 6X	0.0353	2.23	0.0894
Parrot Sequoia	0.0426	2.499	0.0641
Micasense	0.4921	33.62	< 0.001
Sentera 6X	0.4894	33.27	< 0.001
Parrot Sequoia	0.4514	28.7	< 0.001